JGR Biogeosciences

RESEARCH ARTICLE
10.1029/2021JG006605

Key Points:

- Fresh groundwater temperature is a strong control on coastal aquifer reactivity
- Reaction hot spots form within and migrate with warm fresh groundwater masses emplaced during warm months
- Nitrate removal efficiency varies from 5% to 88% for globally diverse thermal regimes with implications under a warming climate

Supporting Information:

Supporting Information may be found in the online version of this article.

Correspondence to:

J. W. Heiss,
james_heiss@uml.edu

Citation:

Cogswell, C., & Heiss, J. W. (2021). Climate and seasonal temperature controls on biogeochemical transformations in unconfined coastal aquifers. *Journal of Geophysical Research: Biogeosciences*, *126*, e2021JG006605. https://doi.org/10.1029/2021JG006605

Received 31 AUG 2021
Accepted 19 NOV 2021

Climate and Seasonal Temperature Controls on Biogeochemical Transformations in Unconfined Coastal Aquifers

Clara Cogswell[1] and James W. Heiss[1]

[1]Department of Environmental, Earth and Atmospheric Sciences, University of Massachusetts Lowell, Lowell, MA, USA

Abstract Coastal aquifers are host to a range of biogeochemical reactions that alter groundwater-derived nutrient, metal, and other chemical loads to coastal ecosystems. Temperature is a strong control on microbially mediated reactions; thus, chemical reactivity in coastal aquifers may vary spatially and temporally with changes to groundwater temperature. In this study, we investigated the influence of global groundwater and sea surface temperature controls and seasonal temperature variability on biogeochemical processing in coastal aquifers using variable-density groundwater flow, heat transport, and reactive transport models. The coupled models showed that nitrate removal efficiency in coastal aquifers increased from 5% to 88% as fresh groundwater temperature increased from 5°C to 35°C, while ocean temperature had a negligible effect on removal efficiency. Transient simulations based on monthly groundwater and ocean temperature measurements showed that denitrification and ammonification hotspots migrated seaward seasonally within warm fresh groundwater masses. The reaction hotspots were separated by colder groundwater emplaced during winter months. The reaction hotspots and nitrate plumes oscillated vertically along horizontal flow paths due to buoyancy effects between warm and cold groundwater. Comparison between transient and temperature-equivalent steady-state models suggests that steady-state models adequately capture mean annual NO_3^- removal, but neglect local reactive transience and changes to plume geometry. The sensitivity analysis provides a first-order estimate of the reactive potential of coastal aquifers considering globally diverse thermal regimes. The findings have implications for regional-scale estimates of groundwater nutrient fluxes and for predicting coastal aquifer reactivity in a warming climate.

Plain Language Summary Nitrate is a groundwater contaminant that enters the subsurface from fertilizer application and septic system release and is later discharged into the ocean at concentrations that are often higher than in river runoff, damaging coastal ecosystems. Microorganisms in porewater beneath the coastline consume nitrate and remove it before it can enter the ocean. The rate that nitrate is consumed depends on temperature, so nitrate removal efficiency may vary seasonally and in different climates. In this study, we used mathematical models to study the influence of climatic and seasonal temperature variations on nutrient cycling in coastal aquifers. Our results indicate that coastal aquifers are more reactive when groundwater temperatures are warmer and that buoyant and highly reactive plumes travel through the aquifer following warm groundwater input. A better understanding of the influence of temperature on coastal aquifer reactivity is essential for the long-term maintenance of coastal ecosystems and water resources and will aid in predicting future responses to climate change.

1. Introduction

Submarine groundwater discharge is an important pathway for land-derived nutrients and contaminants to near-shore marine environments, potentially rivaling riverine nutrient inputs on a regional scale (Burnett et al., 1999; Moore, 1999; Slomp & Van Capellan, 2004; Tanaguchi et al., 2002). High concentrations of nitrogen (N) in groundwater discharging to the coastal ocean can lead to eutrophication, algal blooms, and hypoxia, negatively impacting coastal ecosystems (Guo et al., 2020; Lecher, et al., 2015; Paerl, 1997). In addition to contributing to algal growth, elevated fluxes of nutrients in submarine groundwater discharge can also affect the distribution of seagrass (Rutkowski et al., 1999), meiofauna assemblages (Grzelak et al., 2018), and at higher trophic levels, fish community composition (Pisternick et al., 2020). However, nutrient transformations along the saltwater-freshwater interface can reduce nutrient loads to surface water (e.g. Kroeger & Charette, 2008). Thus, nutrient cycling

in coastal aquifers can play an important role in regulating coastal ecosystem health and is essential for coastal ecosystem management.

A number of field and modeling studies have investigated N cycling along the saltwater-freshwater interface in coastal aquifers. In Waquoit Bay (Massachusetts, USA), two seaward-flowing plumes with different chemical characteristics have been observed to travel conservatively until being forced to mix due to converging flow near the freshwater discharge zone, driving chemical transformations (Kroeger & Charette, 2008; Spiteri, Slomp, Charette, et al., 2008; Talbot & Kroeger et al., 2003). Farther landward at the same field site, Kroeger and Charette (2008) showed significant nitrate (NO_3^-) removal in a NO_3^- plume in the freshwater aquifer prior to discharge, supported by low concentrations of dissolved oxygen. In these anoxic porewater environments on the freshwater side of the saltwater-freshwater interface, N is removed primarily through denitrification, the reduction of NO_3^- and nitrite (NO_2^-) to dinitrogen gas (N_2) (Kroeger & Charette, 2008). Seasonality can affect the timing and magnitude of nutrient loading to coastal surface water, as flow paths and residence times respond to changes in the land-sea hydraulic gradient (Gonneea & Charette, 2014). These studies indicate that freshwater flow near the saltwater-freshwater interface can support varying denitrification, nitrification, and mineralization pathways prior to efflux.

Temperature is an important control on groundwater flow and biogeochemical activity in shallow unconfined aquifers due its effect on fluid viscosity and microbial reaction kinetics. Pu et al. (2020) conduced laboratory tank experiments and used numerical variable-density flow and heat transport models of an unconfined coastal aquifer without tidal influence and showed that the saltwater-freshwater interface shifted seaward with an increase in seawater temperature or a decrease in fresh groundwater temperature. Temperature controls on flow and salt transport have also been investigated in beach aquifers. Nguyen et al. (2020) revealed that tidally induced seawater circulation in intertidal aquifers increases up to 40% when seawater temperature is 15°C warmer than fresh groundwater compared to the case of equal temperatures. Fewer studies have considered the role of temperature on biogeochemical transformations in shallow groundwater-surface water exchange zones. Zheng et al. (2016) numerically simulated heat transport and temperature-dependent reaction kinetics in a stream bedform and showed that a 30°C increase in porewater temperature from 5°C to 35°C resulted in an order of magnitude higher denitrification rates. More efficient NO_3^- consumption in warmer temperature scenarios led to a shallower denitrification zone. In beach aquifers, lower porewater temperatures can decrease respiration rates (e.g. Degenhardt et al., 2020). For instance, on Spiekeroog Island, Germany, seasonal changes in beach porewater temperature have been linked to seasonality in porewater dissolved O_2 concentrations (Waska et al., 2019) and microbial activity (Ahrens et al., 2020). Seasonal groundwater temperatures have also been suggested to control aerobic respiration rates in a beach in France (Charbonnier et al., 2013; Charbonnier, Anschutz, et al., 2016; Charbonnier, Lavesque, et al., 2016). However, to our knowledge, no study has systematically investigated the temperature dependence of N cycling within coastal aquifers. Porewater temperature is likely an important control on coastal aquifer reactivity due to the strong influence of temperature on the kinetic energy of reactants (Dawson & Murphy, 1972). Additionally, Benz et al. (2017) compiled a global groundwater temperature data set of satellite-derived temperature measurements and indicated that a wide range of coastal groundwater temperatures exist across climates; thus, the reactive potential of coastal aquifers is likely to vary along the global coast.

The goal of this study was to investigate the role of global and seasonal variability in groundwater and surface water temperatures on N cycling and NO_3^- removal efficiency along the saltwater-freshwater interface in coastal aquifers. To investigate links between temperature and aquifer biogeochemistry, we used variable-density groundwater flow, heat transport, and reactive transport models with global groundwater and coastal ocean temperature data sets along with measured groundwater and surface water temperatures. We hypothesized that biogeochemical reactivity and solute transport patterns that arise from temperature-controlled density-dependent flow and reaction kinetics lead to temporal variability in coastal aquifer nitrate removal efficiency and spatial variability in the reactive potential of coastal aquifers along coastlines. The results showed that nutrient processing along the saltwater-freshwater interface in warmer climates and during warmer months was higher than in colder climates and during colder months, and that reaction hotspots traveled buoyantly through the aquifer within seasonal warm groundwater masses.

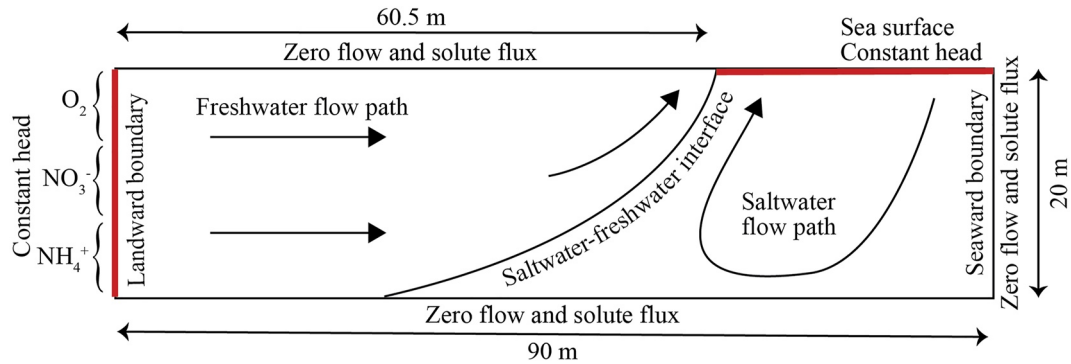

Figure 1. Conceptual diagram of the model domain and generalized flow paths in an unconfined coastal aquifer. The red boundaries represent boundaries with constant hydraulic head, specified concentrations, and specified temperature. In the transient model, the temperature at the red boundaries varied seasonally.

2. Methods

2.1. Numerical Simulations

Variable-density groundwater flow and salt and heat transport were simulated using the numerical finite-difference model SEAWAT v4.0 (Langevin et al., 2007), which couples the groundwater flow equation in MODFLOW-2000 (Harbaugh et al., 2000) with the advective-dispersive transport model MT3DMS (Zheng & Wang, 1999). The flow field generated by SEAWAT was coupled to the multispecies reactive transport model PHT3D v2.13 (Prommer & Post, 2002) to simulate temperature-dependent biogeochemical processing of solutes transported in porewater by advection and dispersion. The model represented a shore-perpendicular cross section of a homogeneous and isotropic coastal aquifer that extended 60.5 m landward of the shoreline, 29.5 m offshore, and to a depth of 20 m below sea level (Figure 1). The model grid was uniform ($\Delta x = 0.5$m, $\Delta y = 0.5$m) and was 40 cells deep by 180 cells long. All simulations used the same model domain parameterized for a generic coastal aquifer, with flow and transport boundary conditions adopted from Spiteri, Slomp, Tuncay, et al. (2008) to loosely reflect flow conditions and N speciation at Waquoit Bay, Massachusetts, USA.

2.2. Groundwater Flow and Heat Transport Models

We performed twenty-two steady-state simulations and one transient simulation. In all models, the landward vertical boundary was assigned a constant hydraulic head of 0.53 m above mean sea level and a constant salinity of 0 ppt. The hydraulic head at the landward boundary was kept constant across all steady-state models to isolate the effects of temperature on biogeochemical processing in the aquifer. A constant hydraulic head representing mean sea level was applied to cells along the aquifer-ocean interface. These cells were assigned a constant salinity of 35 ppt. The outflowing portions of the aquifer-ocean interface were specified as a zero-concentration gradient boundary for both salinity and temperature. The non-inundated top of the models and the bottom and seaward vertical boundaries were set as zero flow and zero salt and heat flux. The permeability was set to 1.05 x 10^{-11} m^2.

Salt concentration and temperature were related to fluid density in the equation of state (Thorne et al., 2006):

$$\rho(C,T) = \rho_f + \frac{\partial \rho}{\partial \mathrm{C}} C + \frac{\partial \rho}{\partial \mathrm{T}} T \quad (1)$$

where ρ_f is the reference density of the fluid (1,000 kg/m^3), $\frac{\partial \rho}{\partial \mathrm{C}} = 0.71$, $\frac{\partial \rho}{\partial \mathrm{T}} = -0.375$ kg/m^3/°C, and C (ppt) and T (°C) are the salinity and temperature of the porewater, respectively.

Fluid viscosity μ (kg/m/s) was related to temperature T (°C) following Hughes and Stanford (2004):

$$\mu = 239.4 \times 10^{-7} \times 10^{\frac{248.37}{T+133.15}} \quad (2)$$

Heat transport is mathematically analogous to advection and dispersion for solute transport and is retarded relative to conservative transport due to thermal exchange between the porewater and solid matrix. The retardation factor R is defined as

$$R = 1 + \frac{\rho_b}{\theta} K_{DT} \quad with \quad \rho_b = \rho_s \ (1 - \theta) \quad (3)$$

and

$$K_{DT} = \frac{c_s}{\rho_b c_f} \quad (4)$$

where ρ_b is the bulk density (kg/m^3), θ is porosity (-), K_{DT} is the thermal distribution coefficient (m^3/kg), ρ_s is the solid matrix density (kg/m^3). c_s is the specific heat of the solid (J/(kg°C)), and c_f is the specific heat of the fluid (J/(kg°C)). A linear isotherm was assumed for sorption. Thermal conduction is similar to molecular diffusion; thus, the thermal diffusivity D_{MT} (m^2/d) is defined as

$$D_{MT} = \frac{\gamma_b}{\theta \rho_f c_f} \quad (5)$$

where γ_b is the thermal conductivity of the solid. Standard parameter values were used in the flow and heat transport models, including thermal diffusivity (0.156 m^2/d), bulk thermal conductivity (2.3 W/(m°C)), and specific heat capacity of the solid (860 J/(kg°C)) and fluid (4,183 J/(kg°C)) (Table 1; Hughes & Stanford, 2004; Vandenbohede & Lebbe, 2011; Voss & Provost, 2010). The flow field from SEAWAT is read by PHT3D to drive the transport of reactive solutes; however, concentrations in SEAWAT cannot be directly incorporated into the rate expressions in PHT3D. Therefore, for each model case, heat transport was also simulated in PHT3D using identical heat transport parameter values.

2.3. Temperature Boundary Conditions: Steady-State and Transient Models

We ran three sets of steady-state models to quantify biogeochemical reactivity for the range of thermal conditions present along the global coast (Table S1 in Supporting Information S1). The temperatures applied to the landward vertical and ocean boundaries were adopted from Nguyen et al. (2020) and Pu et al. (2020) who performed a global analysis of coastal groundwater and nearshore surface water temperatures using data in Benz et al. (2017) and Locarnini et al. (2013). The analysis found that the mean annual coastal groundwater temperature ranges from 5 to 35°C globally with a few areas (e.g., the Horn of Africa) reaching 40°C (Nguyen et al., 2020; Pu et al., 2020). Nearshore sea surface temperatures exhibit a similar global pattern; however, local groundwater and seawater temperatures diverge due in part to ocean circulation patterns, upwelling zones, and climate, leading to groundwater-ocean temperature contrasts ranging from 0 to 15°C (Nguyen et al., 2020; Pu et al., 2020). The temperature of inflowing fresh groundwater and seawater in our first model set (GWa) was uniform and increased from 5 to 35°C. The second model set (GWb) considered variability in fresh groundwater temperature only; inflowing fresh groundwater temperature increased from 5 to 35°C, while seawater temperature was constant at 20°C. Models in set three (SST) were assigned a constant fresh groundwater temperature of 20°C, while the sea surface temperature increased from 5 to 35°C.

The transient model setup was designed to investigate the influence of seasonal variability in groundwater and surface water temperature on aquifer reactivity. The model was assigned the same flow and salt transport boundary conditions as the steady-state models and incorporated seasonal temperature variability in the ocean and groundwater. Time-varying groundwater and seawater temperatures were assigned to the landward vertical and aquifer-ocean interface boundaries, respectively, using 12 monthly stress periods per year. Temperatures assigned to the boundaries were assigned according to field measurements conducted at Waquoit Bay National Estuarine Research Reserve, Massachusetts, USA (see Supplemental Information for sampling details). Briefly, we conducted monthly sampling of porewater from ports along a 9-m-deep sampler in the freshwater aquifer for one year. The measurements revealed nearly vertical temperature profiles throughout the

Table 1
Model Parameters Used in the Flow, Heat Transport, and Biogeochemical Models

Symbol	Parameter	Value	Reference
α_L	Longitudinal dispersivity	0.5 m	Gelhar et al. (1992)
α_T	Transverse dispersivity	0.05 m	Gelhar et al. (1992)
θ	Porosity	0.3	
ρ_s	Solid matrix density	2801 kg/m^3	Approx. value for sand
c_f	Specific heat of fluid	4183 J/(kg°C)	Approx. value for water
c_s	Specific heat of solid	860 J/(kg°C)	Approx. value for sand
K_{DT}	Thermal distribution coefficient	2.06×10^{-4} m^3/kg	Calculated
γ_b	Bulk thermal conductivity	2.3 W/(m°C)	Nguyen et al. (2020)
D_{MT}	Thermal diffusivity	0.156 m^2/d	Calculated
X	Microbial biomass	4.2x10^{-5} (M)	Gu et al. (2007); Knights et al. (2017)
V_{ar}	Maximum specific O_2 reaction rate at 20°C	2.8×10^{-5} (s^{-1})	Zarnetske et al. (2012)
V_{nit}	Maximum specific NH_4^+ reaction rate at 20°C	1×10^{-4} (s^{-1})	Zarnetske et al. (2012)
V_{den}	Maximum specific NO_3^- reaction rate at 20°C	1.4×10^{-6} (s^{-1})	Sheibley et al. (2003)
$\beta_{ar_{O_2}}$	Stoichiometric coefficient: aerobic respiration (O_2)	1	Stoichiometry
$\beta_{ar_{DOC}}$	Stoichiometric coefficient: aerobic respiration (DOC)	1	Stoichiometry
$\beta_{nit_{O_2}}$	Stoichiometric coefficient: nitrification (O_2)	2	Stoichiometry
$\beta_{nit_{NO_3}}$	Stoichiometric coefficient: nitrification (NO_3^-)	1	Stoichiometry
$\beta_{nit_{NH_4}}$	Stoichiometric coefficient: nitrification (NH_4^+)	1	Stoichiometry
$\beta_{den_{NO_3}}$	Stoichiometric coefficient: denitrification (NO_3^-)	0.8	Stoichiometry
$\beta_{den_{DOC}}$	Stoichiometric coefficient: denitrification (DOC)	1	Stoichiometry
$\beta_{ar_{NH_4}}$	Stoichiometric coefficient: aerobic ammonification	0.104	Stoichiometry
$\beta_{den_{NH_4}}$	Stoichiometric coefficient: anaerobic ammonification	0.104	Stoichiometry
K_{DOC}	Half-saturation constant for DOC	7.23×10^{-4} (M)	Knights et al. (2017); Zarnetske et al. (2012)
K_{NH4}	Half-saturation constant for NH_4^+	3.07×10^{-5} (M)	Knights et al. (2017); Zarnetske et al. (2012)
K_{O2}	Half-saturation constant for O_2	3.30×10^{-4} (M)	Knights et al. (2017); Zarnetske et al. (2012)
K_{NO3}	Half-saturation constant for NO_3^-	1.18×10^{-4} (M)	Knights et al. (2017); Zarnetske et al. (2012)
K_I	Inhibition constant	1.50×10^{-5} (M)	Knights et al. (2017); Zarnetske et al. (2012)
$E_{(Nitrification)}$	Activation energy nitrification	162,000 J/mol	Sheibley et al. (2003)
$E_{(Denitrification)}$	Activation energy denitrification	97,300 J/mol	Sheibley et al. (2003)
$E_{(Aerobic\ respiration)}$	Activation energy aerobic respiration	60,000 J/mol	Zheng et al. (2016)
R	Ideal Gas Constant	8.31 J/mol	

year, indicating that horizontal flow dominates over recharge-induced vertical flow at the Waquoit Bay field site (Figure S1 in Supporting Information S1). Thus, the average groundwater temperature measured during each month (range 7.7°C to 17.6°C) was applied to the corresponding monthly stress period at the left model boundary. Monthly surface water temperatures were assigned to the ocean boundary. The 12 monthly stress periods were repeated until temperatures in the aquifer reached dynamic steady state (year 7) to ensure that initial conditions had no effect on model results. Simulated temperatures, concentrations, and reactivity for year 8 are reported. An additional steady-state "temperature-equivalent" simulation was performed with boundaries set to the measured mean annual fresh groundwater and ocean temperature at Waquoit Bay to assess the impor-

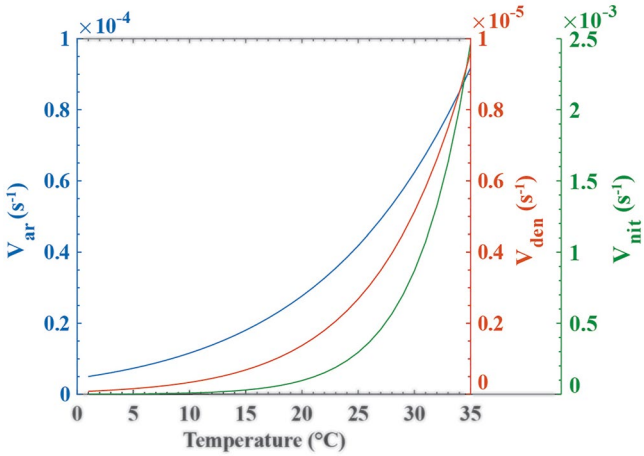

Figure 2. Aerobic respiration (V_{ar}), nitrification (V_{nit}), and denitrification (V_{den}) rate constants as a function of temperature plotted using the Arrhenius equation (Equation 11).

tance of incorporating seasonal temperature variability in biogeochemical models of coastal aquifers. Comparison of model results from the transient model and the "temperature-equivalent" model (Section 3.2.1 and 3.2.3) confirmed that the use of steady-state models in the global assessment is a reasonable approach for modeling spatial variability in aquifer reactivity along coastlines.

2.4. Reactive Transport Model

The model considered the key solutes involved in N cycling in coastal aquifers: DOC, dissolved oxygen (O_2), NO_3^-, and NH_4^+. These solutes were incorporated into a reaction network to simulate aerobic respiration, denitrification, nitrification, and aerobic and anaerobic mineralization. The governing reaction equations used in the model were adopted from previous studies investigating N cycling in shallow unconfined aquifers (e.g., Knights et al., 2017; Zarnetske et al., 2012) and follow the classical cascade of electron acceptors using multiple Monod kinetics (Molz et al., 1986):

$$R_{O_2} = -V_{ar} X \beta_{ar_{O_2}} \left(\frac{DOC}{K_{DOC} + DOC}\right)\left(\frac{O_2}{K_{O_2} + O_2}\right) - V_{nit} X \beta_{nit_{O_2}} \left(\frac{NH_4}{K_{NH_4} + NH_4}\right)\left(\frac{O_2}{K_{O_2} + O_2}\right) \quad (6)$$

$$R_{NO_3} = V_{nit} X \beta_{nit_{NO_3}} \left(\frac{NH_4}{K_{NH_4} + NH_4}\right)\left(\frac{O_2}{K_{O_2+O_2}}\right) - V_{den} X \beta_{den_{NO_3}} I \left(\frac{DOC}{K_{DOC} + DOC}\right)\left(\frac{NO_3}{K_{NO_3} + NO_3}\right) \quad (7)$$

$$R_{NH_4} = -V_{nit} X \beta_{nit_{NH_4}} \left(\frac{NH_4}{K_{NH_4} + NH_4}\right)\left(\frac{O_2}{K_{O_2+O_2}}\right) + V_{ar} X \beta_{ar_{NH_4}} \left(\frac{DOC}{K_{DOC} + DOC}\right)\left(\frac{O_2}{K_{O_2+O_2}}\right) + V_{den} X \beta_{den_{NH_4}} I \left(\frac{DOC}{K_{DOC} + DOC}\right)\left(\frac{NO_3}{K_{NO_3} + NO_3}\right) \quad (8)$$

$$R_{DOC} = -V_{ar} X \beta_{ar_{DOC}} \left(\frac{DOC}{K_{DOC} + DOC}\right)\left(\frac{O_2}{K_{O_2} + O_2}\right) - V_{den} X B_{den_{DOC}} I \left(\frac{DOC}{K_{DOC} + DOC}\right)\left(\frac{NO_3}{K_{NO_3+NO_3}}\right) \quad (9)$$

$$I = \frac{K_I}{K_I + O_2} \quad (10)$$

where R_{O_2}, R_{NO_3}, R_{NH_4}, and R_{DOC} (M^{-1}) are the net reaction rates of the i-th solute, V_i (s^{-1}) is the maximum specific uptake rate of the i-th solute, X (M) is the microbial biomass, and β_{r_i} (-) is the stoichiometric coefficient for reaction r and solute i. The inhibition of denitrification in the presence of O_2 is represented in Equation 10 and incorporated into the denitrification terms in Equations 7–9 (Widdowson et al., 1988). The model parameter values are shown in Table 1.

The influence of temperature on reaction rates was incorporated into the reactive transport model using the Arrhenius equation (Dawson and Murphy, 1972):

$$V(T) = Ae^{-E/CT} \quad (11)$$

where V (M^{-s}) is the reaction rate constant (e.g., V_{ar}, V_{nit}, and V_{den}), T is temperature in Kelvin (K), A is the pre-exponential factor, E (J/mol) is the activation energy, and C (J/mol-K) is the ideal gas constant. Rate constants were dynamically calculated within the model for each time step according to the temperature of the porewater at each model cell. Table 1 lists the rate constants at 20°C and the activation energies for aerobic respiration, nitrification, and denitrification. Rate constants for aerobic respiration, denitrification, and nitrification increase across the full temperature range considered in the simulations (Figure 2).

Constant concentrations of DOC, O_2, NO_3^-, and NH_4^+ were assigned to the aquifer-ocean interface and landward boundary. The specified concentrations and depth of inflowing nutrients at the left boundary (NO_3^-: 2.5 x 10^{-4} mol/L; NH_4^+: 2.0 x 10^{-4} mol/L) were adopted from case 3 in Spiteri, Slomp, Tuncay, et al. (2008). The middle third of the boundary served as a source of NO_3^- and the bottom third of the boundary served as a source of NH_4^+, consistent with the vertical layering of the nutrients measured in other studies (e.g., Figure 1; Erler et al., 2014; Santos et al., 2008). The top third of the landward boundary served as a source of O_2 (5.0 x 10^{-5} mol/L), following previous studies that have measured elevated O_2 levels in the freshwater aquifer (e.g. Kroeger & Charette, 2008; Santos et al., 2008; Tamborski et al., 2017). The bottom two thirds of the landward boundary served as a source of DOC (7.5 x 10^{-4} mol/L), following Spiteri, Slomp, Tuncay, et al. (2008). Seawater was set as a source of DOC (2.0 x 10^{-4} mol/L) and O_2 (1.3 x 10^{-4} mol/L) for inflowing portions of the aquifer-ocean interface.

2.5. Reactivity Metrics

The net mass of NO_3^- removed or produced in the models was calculated as the difference between the denitrification and nitrification rate at each model cell integrated across the model domain. NO_3^- removal efficiency was calculated by dividing the net mass of NO_3^- removed by the mass influx of NO_3^- across the left boundary. The net change in NH_4^+ flux was calculated as the difference between the NH_4^+ influx and outflux divided by the influx.

We used the dimensionless Damköhler number (*Da*) to relate changes in reactivity due to temperature variability to the advective transport rate. The *Da* number signifies the relative balance of reactant supply to microbial demand. A *Da* of 1 indicates that reactant supply is balanced by microbial demand and a *Da* greater than 1 indicates the reactant supply is unable to match microbial demand. Below a *Da* of 1, the supply of reactive species outpaces demand. *Da* is defined as

$$Da = \frac{R_i \cdot L}{v} \tag{12}$$

where R_i (moles/d) is the denitrification rate, L (m) is a characteristic length scale, and v (m/d) is the advective transport rate. A characteristic length scale of 60.5 m was used to quantify the balance of NO_3^- supply-demand along the length of the freshwater flow path.

We quantified the movement of reaction hotspots in the transient model by computing the spatial moments of the aerobic respiration, denitrification, nitrification, and ammonification reaction zones in the freshwater. In a 2D cross section, the centroid (x_c, z_c) coordinates are defined as

$$x_c = \frac{M_{x,1}}{M_{x,0}} \tag{13}$$

$$z_c = \frac{M_{z,1}}{M_{z,0}} \tag{14}$$

where M is the spatial moment in the x or z direction;

$$M_{s,m} = \sum_{i=1}^{N_{node}} s_i^m r_i \tag{15}$$

where $s = x$ or z, $m = 0$ or 1, N_{node} = total number of nodes, and r_i = reaction rate at the ith node.

Lastly, the cross-sectional area of each solute plume was calculated by summing the area of model cells with a concentration higher than 5% of the end-member concentration.

3. Results

3.1. Steady-State Simulations: Spatial Temperature Controls Along Coastlines

3.1.1. Concentration Distributions

The base of the saltwater-freshwater interface in the steady-state simulations migrated landward as seawater temperatures decreased and migrated seaward as freshwater temperatures decreased. These findings are consistent

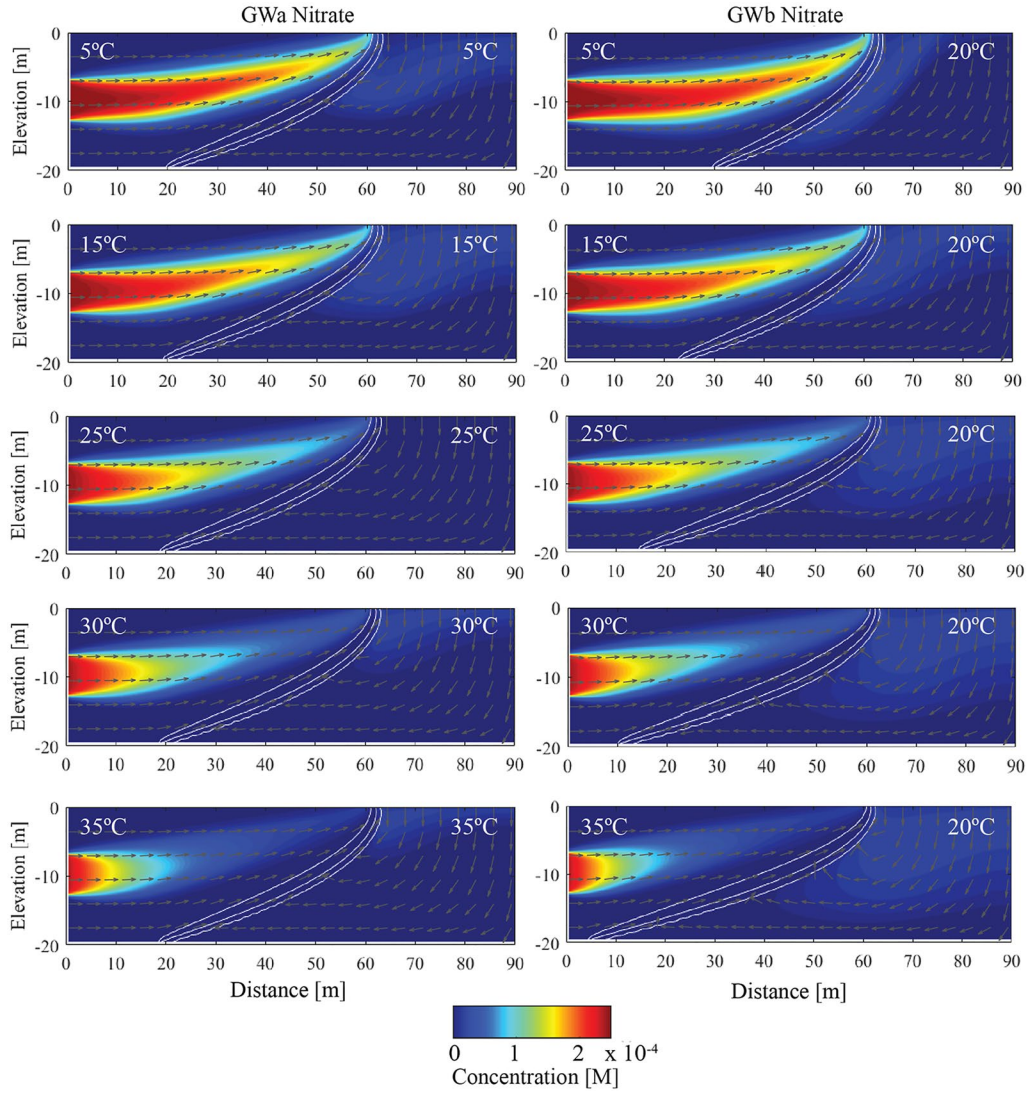

Figure 3. NO_3^- concentrations, salinity, and flow vectors for model sets GWa (left column) and GWb (right column). Fresh groundwater and seawater temperatures are labeled in white. The white contours are the 5%, 50%, and 95% seawater salinity contours. The gray vectors show the normalized flow field.

with Pu et al. (2020) and are expected due to temperature controls on density contrasts between the fresh and saltwater aquifers. In simulations where seawater and freshwater temperatures were equal and varied uniformly (Figure 3; GWa), the density contrast between the freshwater and saline porewater was constant; thus, the base of the interface remained stationary between temperature scenarios (Figure 3; left column). As fresh groundwater temperature increased from 5°C to 35°C in GWb simulations (seawater temperature constant), the base of the interface moved inland 25 m due to an increase in the density ratio between seawater and fresh groundwater (Figure 3; right column).

NO_3^- concentrations in model sets GWa and GWb decreased with an increase in fresh groundwater temperature (Figure 3). The NO_3^- concentration at the fresh discharge zone at a fresh groundwater temperature of 5°C was 41% of the inflowing concentration at the left boundary, which decreased to 17% when the fresh groundwater temperature increased to 35°C. NO_3^- concentrations along the length of the NO_3^- plume in warmer fresh groundwater decreased more rapidly between the landward boundary and discharge zone (Figure 3). Conversely, in scenarios with increasing seawater temperature and a constant fresh groundwater temperature (model set SST), the concentration of discharging NO_3^- was 36% of the inflowing concentration across all model scenarios, indicating that seawater temperature has a negligible effect on NO_3^- consumption (Figure S2 in Supporting Information S1).

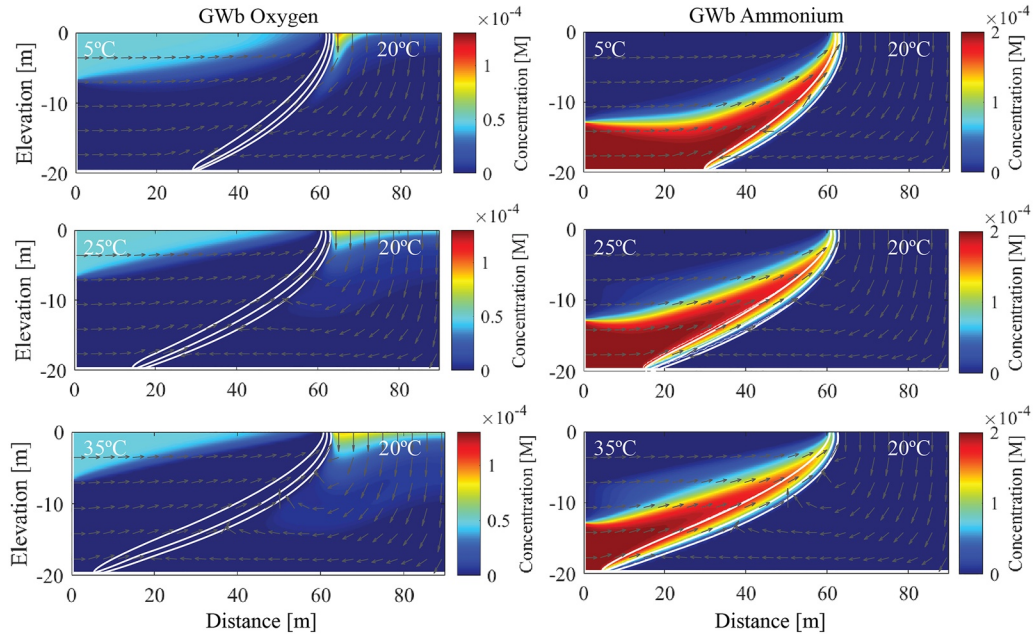

Figure 4. O_2 (left) and NH_4^+ (right) concentrations for a subset of GWb models. Freshwater and seawater temperatures are shown in white text. The white contours are the 5%, 50%, and 95% seawater salinity contours. The gray vectors show the normalized flow field.

These results indicate that fresh groundwater temperature was a more important control on NO_3^- concentrations than seawater temperature, and that fresh groundwater temperature modified NO_3^- concentrations by controlling NO_3^- consumption along fresh groundwater flow paths.

The spatial distribution of dissolved O_2 and NH_4^+ varied across the range of fresh groundwater temperatures due to changes in both chemical transformation rates and the position of the saltwater interface. The oxic zone in GWa (not shown) and GWb models (Figure 4; left column) narrowed vertically seaward of x = ~20 m as O_2 consumption rates increased with fresh groundwater temperature. At the bottom of the aquifer, the NH_4^+ plume was displaced upward as the saltwater interface intruded inland under warmer and less dense fresh porewater (Figure 4; right column). The displacement of the NH_4^+ plume did not occur in cases where fresh groundwater and seawater temperatures increased uniformly because the density contrast across the interface remained constant. The degradation of DOC served as a source of NH_4^+ through ammonification, and the release of NH_4^+ into porewater was higher for warmer groundwater temperatures. This was most evident along the top boundary of the NH_4^+ plume for the warmest fresh groundwater case, where there was a moderate increase in NH_4^+ from x = 0–20 m (Figure 4; row 3).

3.1.2. Reactivity

The spatial distribution of denitrification and ammonification rates illustrates the role of groundwater temperature on controlling the biogeochemical reactivity of the coastal aquifer. Denitrification rates in the landward half of the freshwater aquifer (x = 0–30 m) in GWa and GWb increased with fresh groundwater temperature, regardless of the seawater temperature (Figure 5). NO_3^- consumption rates within this region of the aquifer increased slowly from 5°C to 20°C and then rapidly from 20°C to 35°C owing to the exponential rise in DOC reactivity with an increase in temperature (Figure 2). The highest denitrification rate between x = 0–30 m increased 25.2% from 5°C to 20°C and 57.8% from 20°C to 35°C. Denitrification rates in the seaward half of the freshwater aquifer (x = 30–60.5 m) increased from 5°C to 25°C; however, there was a small decrease in nitrite consumption in that region of the aquifer from 25°C to 35°C. Efficient NO_3^- removal near the landward boundary at 35°C significantly reduced NO_3^- availability closer to the shoreline; thus, NO_3^- supply was unable to match microbial demand and reaction rates decreased seaward of x = 30 m (Figure S3 in Supporting Information S1). The spatial pattern of ammonification was similar to denitrification, as DOC degradation and NH_4^+ production were coupled to NO_3^- reduction (Figure 6). A narrow horizontal strip of

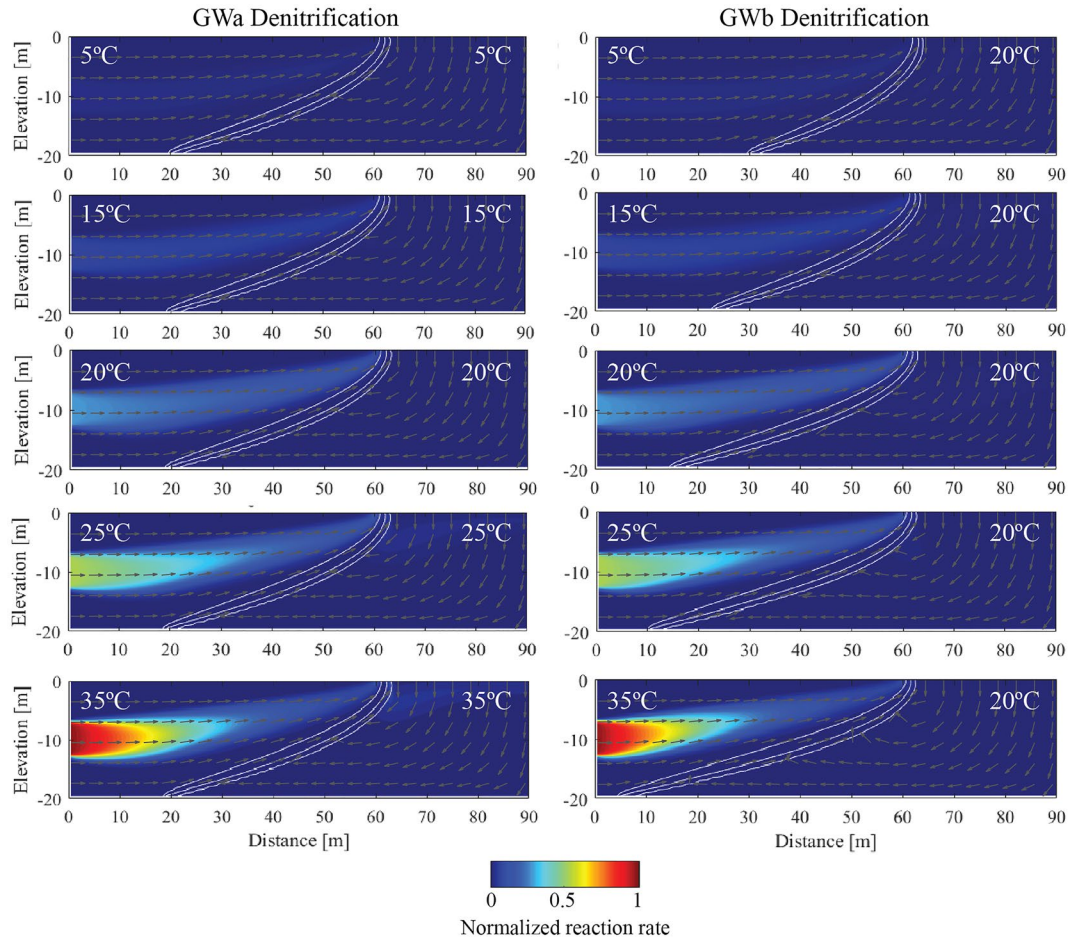

Figure 5. Denitrification rates for model sets GWa and GWb. White contours are 5%, 50%, and 95% seawater salinity contours. The gray vectors show the normalized flow field. Reaction rates are normalized by the maximum reaction rate across all models.

elevated ammonification rates beginning at a depth of 6 m at the left boundary occurred due to mixing between DOC and O_2 plumes, resulting in aerobic respiration and subsequent DOC mineralization and NH_4^+ release.

3.1.3. NO_3^- Removal Efficiency

The model results show that warmer fresh groundwater increased NO_3^- removal efficiency. (Figure 7a-b). In GWa simulations (uniformly increasing fresh groundwater and seawater temperature), NO_3^- removal efficiency increased from 5.2% to 88.3% as temperature rose from 5°C to 35°C (Figure 7a). The trend in NO_3^- removal efficiency for GWb simulations (increasing fresh groundwater temperature, constant 20°C seawater temperature) was similar, with NO_3^- removal efficiency increasing from 3.9% to 88.0% as fresh groundwater temperature increased from 5°C to 35°C (Figure 7b). There was no change in NO_3^- removal efficiency when fresh groundwater temperature was held constant as seawater temperatures increased from 5°C to 35°C (Figure 7c; SST). These results indicate that fresh groundwater temperature was the primary control on NO_3^- processing in the system. Although the toe of the interface moved 20 m seaward as seawater temperature increased in SST simulations (Figure S2 in Supporting Information S1), the corresponding shifts to freshwater flow paths along the interface had negligible influence on NO_3^- attenuation.

We quantified the net change in NH_4^+ to explore the relative balance of ammonification and nitrification within and across thermal regimes. In nearly all models in GWa and GWb, NH_4^+ outflux across the seabed was greater than freshwater NH_4^+ influx (Figure 7d-e). The net change in NH_4^+ flux across the seabed increased from 0.1 to 13.4% and from −1.0 to 17.0% in GWa and GWb model sets, respectively, indicating that DOC

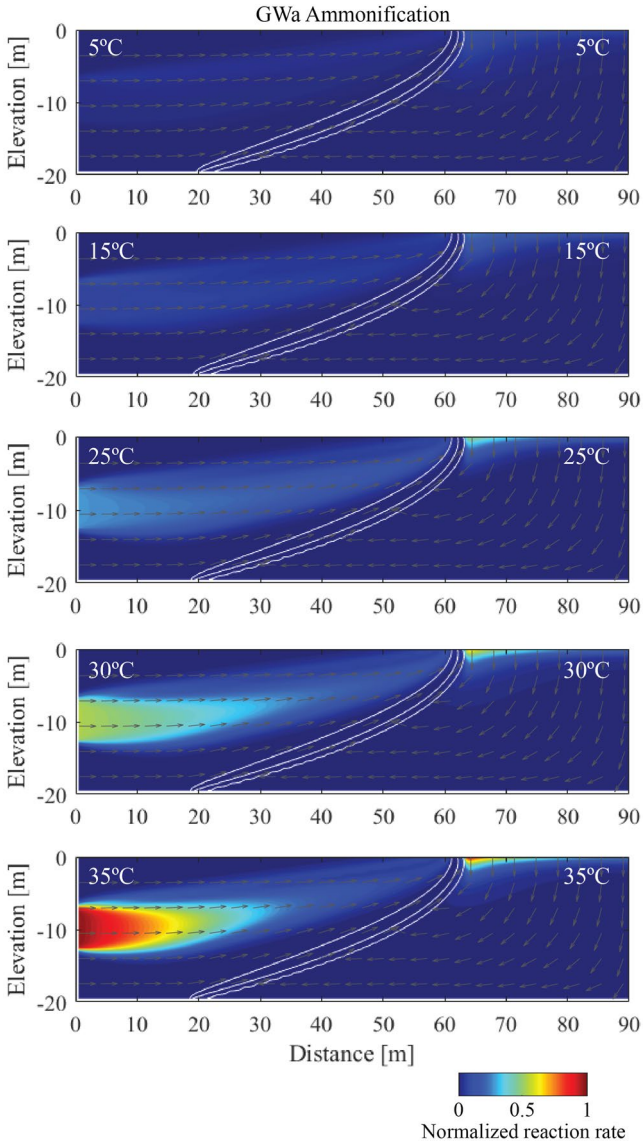

Figure 6. Ammonification rates for GWa models. Fresh groundwater and bay water temperatures increase from 5°C to 35°C. GWb models yielded similar results and are not shown. The white contours are the 5%, 50%, and 95% seawater salinity contours. The gray vectors show the normalized flow field. Reaction rates are normalized by the maximum reaction rate.

degradation and NH_4^+ release increased in warmer fresh groundwater. In GWb (increasing fresh groundwater temperature, constant 20°C seawater), a negative (−1%) net change (net NH_4^+ removal) occurred when the fresh groundwater temperature was between 5 and 10°C (Figure 7e). At these low fresh groundwater temperatures, ammonification was inhibited, while mixing between colder freshwater and warmer 20°C seawater along the shallow portion of the saltwater interface supported nitrification sufficient to result in net NH_4^+ removal; O_2 that recharged across the seabed due to density-driven circulation supported nitrification along the upper interface. SST simulations showed net NH_4^+ production over a narrow range from 3.9% to 1.6% (2.3% change), indicating that the effect of sea surface temperature on density-driven circulation had little influence on NH_4^+ fluxes to surface water.

3.2. Transient Simulation: Seasonal Temperature Controls

3.2.1. Transient Model Solute Concentration Distributions

The transient model results show that the toe of the saltwater-freshwater interface moved only 1-2 m across the base of the aquifer when the temperature of inflowing fresh groundwater and seawater varied seasonally. These interface dynamics are similar to the results of the steady-state GWa models where the interface toe remained stationary as fresh groundwater and seawater temperature increased uniformly. To further assess the importance of incorporating seasonal temperature variability in groundwater flow models of coastal aquifers, we performed a "temperature-equivalent" steady-state simulation. The measured mean annual fresh groundwater and seawater temperatures, 12.3°C and 14.7°C, respectively, were assigned as boundary conditions in a steady-state model. Comparison between the transient model and the "temperature-equivalent" steady-state model showed that the position of the interface along the base of the aquifer was nearly the same (±2 m) in both models and that the mass of saltwater in the aquifer differed by less than 2%. Thus, steady-state (boundary conditions) heat-transport models of coastal aquifers that consider mean annual temperatures can closely approximate the location and dynamics of the saltwater-freshwater interface when temperature is the only controlling factor.

O_2, NO_3^-, and NH_4^+ were transported along undulating flow paths from the landward boundary to the discharge zone (Figure 8). The undulating flow paths formed due to buoyancy forces as warm and cold groundwater masses moved through the system. Warm buoyant porewater lifted the oxic, NO_3^-, and NH_4^+ plumes upward, while adjacent cooler and denser zones coincided with sinking groundwater and a downward shift in the plumes (Figures 8 and 10). Warm water that entered the aquifer in July caused the NO_3^- plume to undulate up to 5 m as warm groundwater flowed through the aquifer to the discharge zone. The seaward movement and changes to the strength of the undulation along the NO_3^- plume coincided with changes to the plume area (Figures 8 and 9b). For example, the NO_3^- plume decreased seasonally in size by 15 m^2 from March to September as the seaward half of the plume straightened until a lagged pulse of warm water from summer entered the aquifer and caused the NO_3^- plume to locally uplift near x = 10 m, leading to an increase in plume area starting in October. At depth, the NH_4^+ plume decreased in size from spring to summer as a result of a downward shift in the overlying NO_3^- plume (Figures 8 and 9c).

O_2 concentrations on the saltwater side of the interface varied in response to changes in aerobic respiration rates (Figure 8; left column). High rates of density-driven inflow and circulation between the top of the interface and 10 m seaward (x = 60–70 m) maintained elevated O_2 concentrations below the seabed. The O_2 concentrations

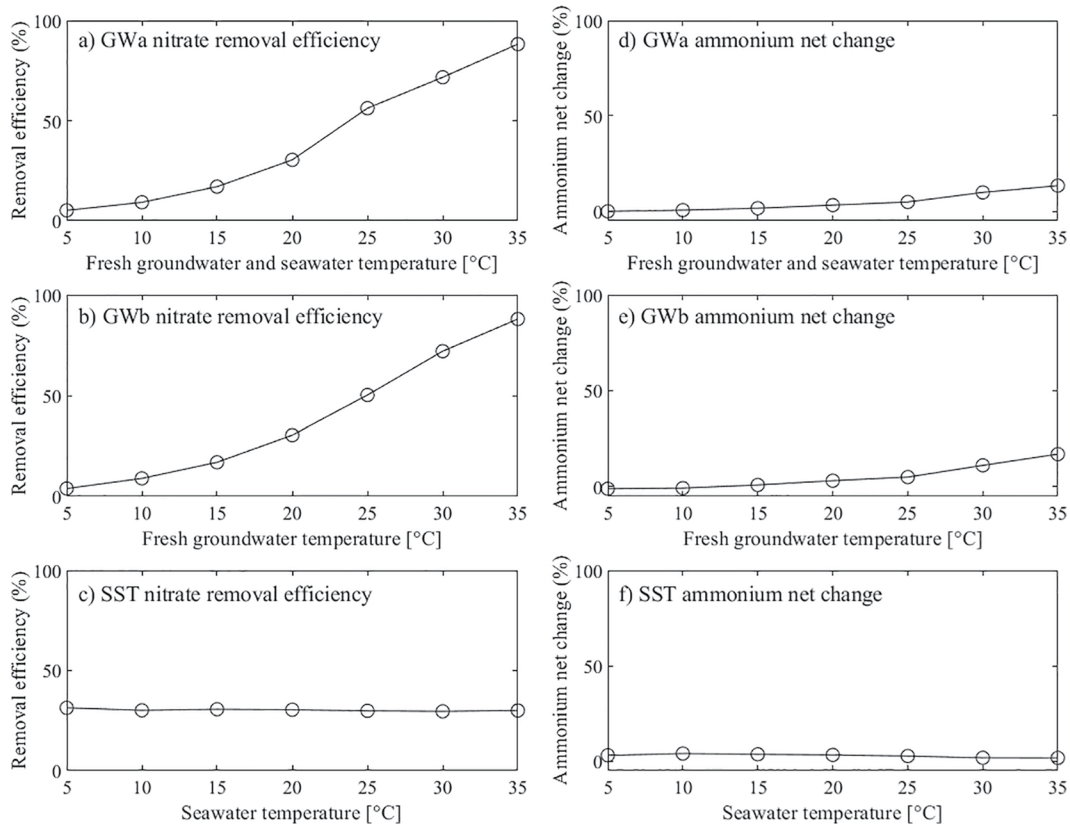

Figure 7. NO_3^- removal efficiency and net change in NH_4^+ for GWa, GWb, and SST model sets. Left column: NO_3^- removal efficiencies. Right column: NH_4^+ net change. The seawater temperature in panels (b) and (e) is constant at 20°C. The fresh groundwater temperature in panels (c) and (f) is constant at 20°C. A positive NH_4^+ net change indicates production, negative signifies net NH_4^+ consumption.

were highest in March when aerobic respiration was inhibited by colder inflowing seawater. In September, warm seawater from the summer months occupied the upper portion of saltwater side of the interface. The warmer porewater supported higher aerobic respiration rates, resulting in lower O_2 concentrations.

3.2.2. Transient Model Reactivity Distributions

Periods of warm fresh groundwater input corresponded to a zone of enhanced denitrification at the left boundary, which moved seaward with the warm fresh groundwater over a period of 335 days (Figure 10). Ammonification in the denitrification hotspot was elevated due to the higher DOC oxidation rates in the warm fresh groundwater (Figure 10; column 2). The intensity of the ammonification and denitrification hotspots subsided as they migrated seaward due to a decrease in reactant availability along the flow path. A thin horizontal zone of aerobic respiration formed where O_2 near the ground surface overlapped with DOC at depth (Figure 10; column 3). Farther seaward, density-driven recharge of seawater across the seabed supplied O_2 and DOC to the saltwater side of the interface, which maintained elevated aerobic respiration rates. Nitrification occurred within the same offshore area as the aerobic respiration zone, owing to the coupled release of NH_4^+ from DOC degradation (Figure 10; column 4). While individual denitrification hotspots migrated from the left model boundary to the discharge zone, the denitrification zone centroid exhibited less motion (Figure S4 in Supporting Information S1). The explanation for the disconnect between individual hotspot movement and the reaction zone centroid is the frequent occurrence of two separate denitrification hotspots along the freshwater flow path (Figure 10). As one hotspot exited the aquifer, a second emerged from the left boundary, which led to a computed centroid location between the two hotspots and reduced centroid movement.

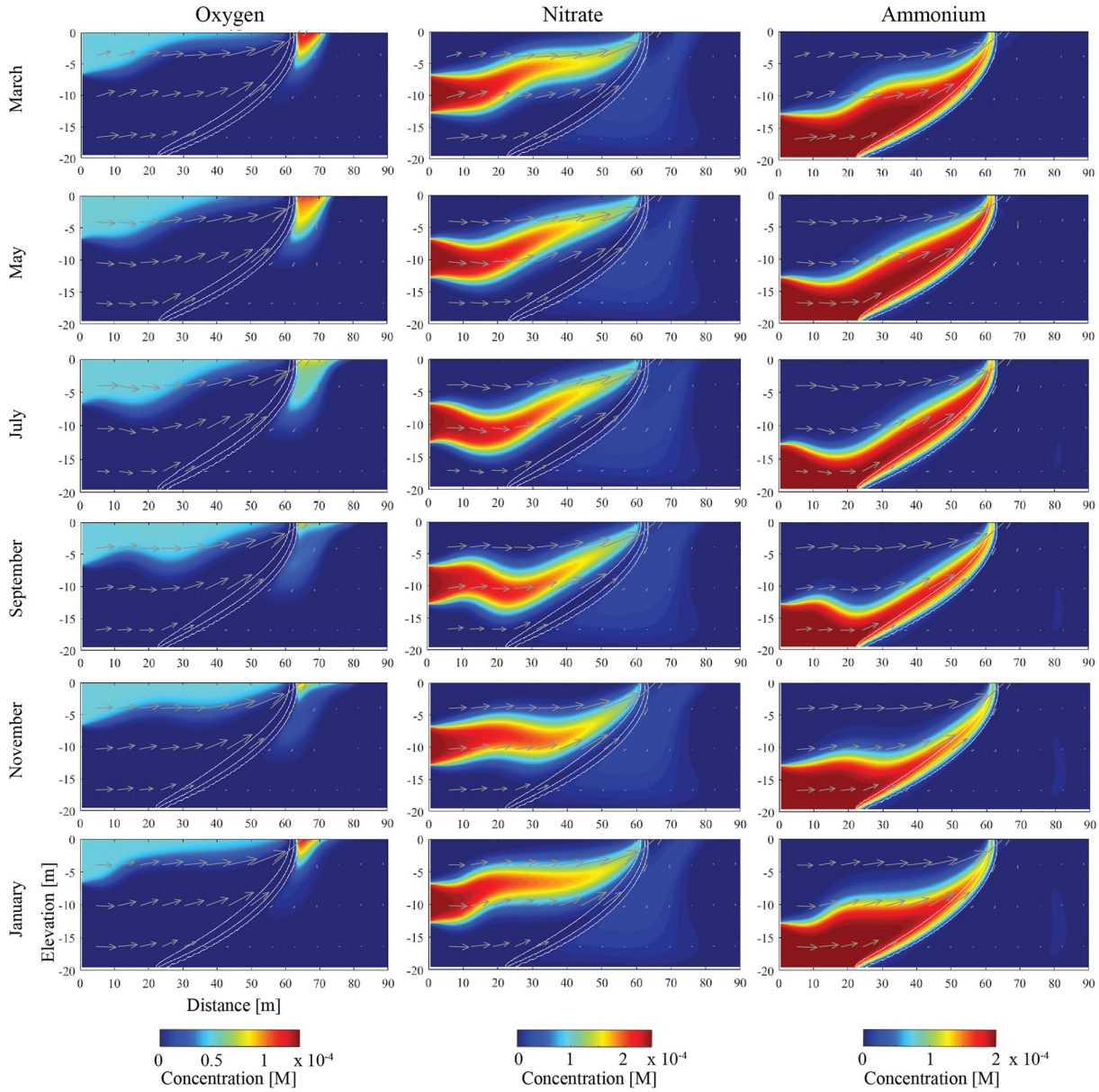

Figure 8. Bimonthly simulated concentrations from the transient model. Left: O_2. Middle: NO_3^-. Right: NH_4^+. The white contours are the 5%, 50%, and 95% seawater salinity contours. The gray vectors show the flow field.

3.2.3. Transient Model NO_3^- Removal Efficiency

We computed NO_3^- removal efficiency and the mean fresh groundwater temperature in the aquifer for each simulated time step to further analyze the influence of seasonal temperature variability on N cycling. NO_3^- removal efficiency oscillated seasonally with fresh groundwater temperature, peaking at 13.8% in summer at 13.0°C and reaching a low of 12.5% in winter at 11.5°C (Figure 11). The small 1.3% range was due to the effect of averaging temperature and integrating the mass of NO_3^- removed across the domain, which dampened variability along the freshwater flow paths shown in Figure 9. The temporal trend was similar to the findings of Addy et al. (2005) where a seasonal effect on denitrification was measured in a salt marsh aquifer, with higher rates in summer. Ahrens et al. (2020) similarly observed increased respiration rates in a coastal aquifer in summer.

The transient model results were compared to the "temperature-equivalent" steady-state model to assess the importance of incorporating seasonal temperature variability in models when estimating NO_3^- removal efficiency. NO_3^-

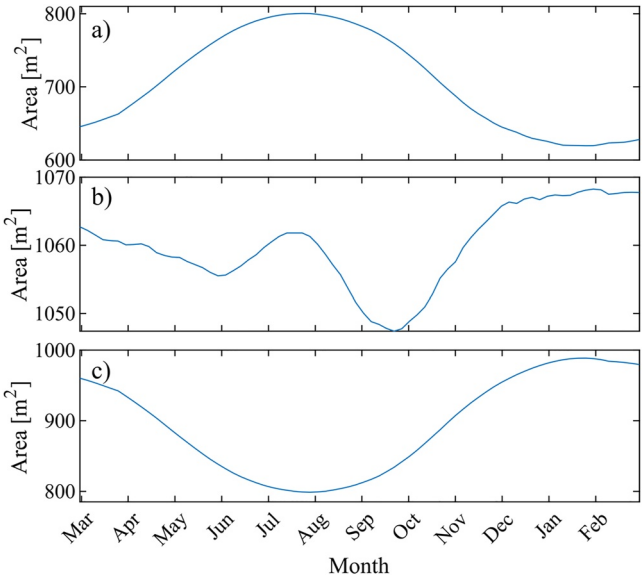

Figure 9. Area of the O_2, NO_3^-, and NH_4^+ plumes on the freshwater side of the saltwater interface over a period of one year.

removal efficiency in the "temperature-equivalent" steady-state model was 9.7%, which is similar to the mean annual removal efficiency (13.2%) in the transient model. These results suggest that steady-state models with site-specific mean annual fresh groundwater and ocean temperatures applied as boundary conditions can be used to approximate mean annual NO_3^- removal efficiency.

3.3. Temperature and Reactant Supply and Demand

Fresh groundwater temperature controlled the relative balance of NO_3^- supply and microbial uptake through its influence on the reaction rate. In model cases where fresh groundwater and seawater temperatures increased uniformly (GWa) from 5°C to 20°C, *Da* was less than 1 throughout the freshwater aquifer, indicating that colder groundwater temperatures maintained low enough denitrification rates to allow NO_3^- to be transported to the discharge zone more conservatively (Figure S5A–D in Supporting Information S1). From 25°C to 35°C (Figure S5E–G in Supporting Information S1), *Da* in sections of the NO_3^- plume was greater than 1 as NO_3^- supply was unable to match higher microbial demand in warmer fresh groundwater. The spatial average (0.09–0.96) and variability of *Da* increased as fresh groundwater temperature rose from 5°C to 35°C (Figure 12a). Thus, while localized areas with $Da > 1$ formed in the aquifer, the broader system was rate-limited across the full range of thermal conditions tested, with NO_3^- consumption approaching supply ($Da = 1$) only for the case with the warmest fresh groundwater temperature. The variability and spatial average of *Da* were the same across SST cases, further indicating the negligible effect of sea surface temperature on the consumption of land-derived NO_3^- prior to discharge (Figure 12b).

4. Discussion

4.1. Effects of the Position of the Saltwater Interface

Model sensitivity tests show that fresh groundwater temperature exerts greater control over aquifer reactivity than seawater temperature. Such influences are expected, as inflowing fresh groundwater served as a source of nutrients to the aquifer, which is common in many coastal systems (e.g., Kroeger & Charette, 2008; Beck et al., 2017; Kim et al., 2017). While seawater temperature was not important to NO_3^- removal, it affected the depth of the contaminant plumes by controlling the amount that contaminants were displaced upward by intruding seawater prior to discharge (Figure 4). This temperature-controlled saltwater intrusion and its effect on lifting groundwater contaminants closer to the land surface may have implications for nutrient and other contaminate fluxes to coastal streams and lakes. A recent global assessment of total nearshore (onshore and offshore) groundwater discharge suggests that 66% of coastal groundwater discharges onshore landward of the shoreline (Luijendijk et al., 2020). The onshore discharge contributes to surface runoff, base flow, lakes, and wetlands before reaching the coast (Bokuniewicz, 1992). This suggests that water quality of coastal aquatic systems may be at a reduced or heightened risk of impairment depending on the depths of contaminant plumes and present and future temperature contrasts between groundwater and the coastal ocean.

4.2. Implications for Measurements

Porewater incubation experiments have been used to quantify reaction rates in coastal aquifers (e.g., Lecher et al., 2015; Kim et al., 2017). In laboratory incubations, porewater is often incubated at a temperature that is different from in situ temperatures. The incubated reaction rates are then converted to in situ reaction rates using measured porewater temperatures and the Arrhenius equation. The transient model, which was assigned boundary conditions based on field measurements, suggests that groundwater temperature can be highly variable spatially and temporally near the saltwater interface. This suggests that the location where porewater is sampled for incubation can dictate whether the sample is from a colder or warmer groundwater mass. Therefore, incubated reaction rates that are converted to in situ reaction rates using porewater temperatures measured in warmer regions and then spatially or temporally extrapolated may overestimate the reactivity of the broader freshwater aquifer.

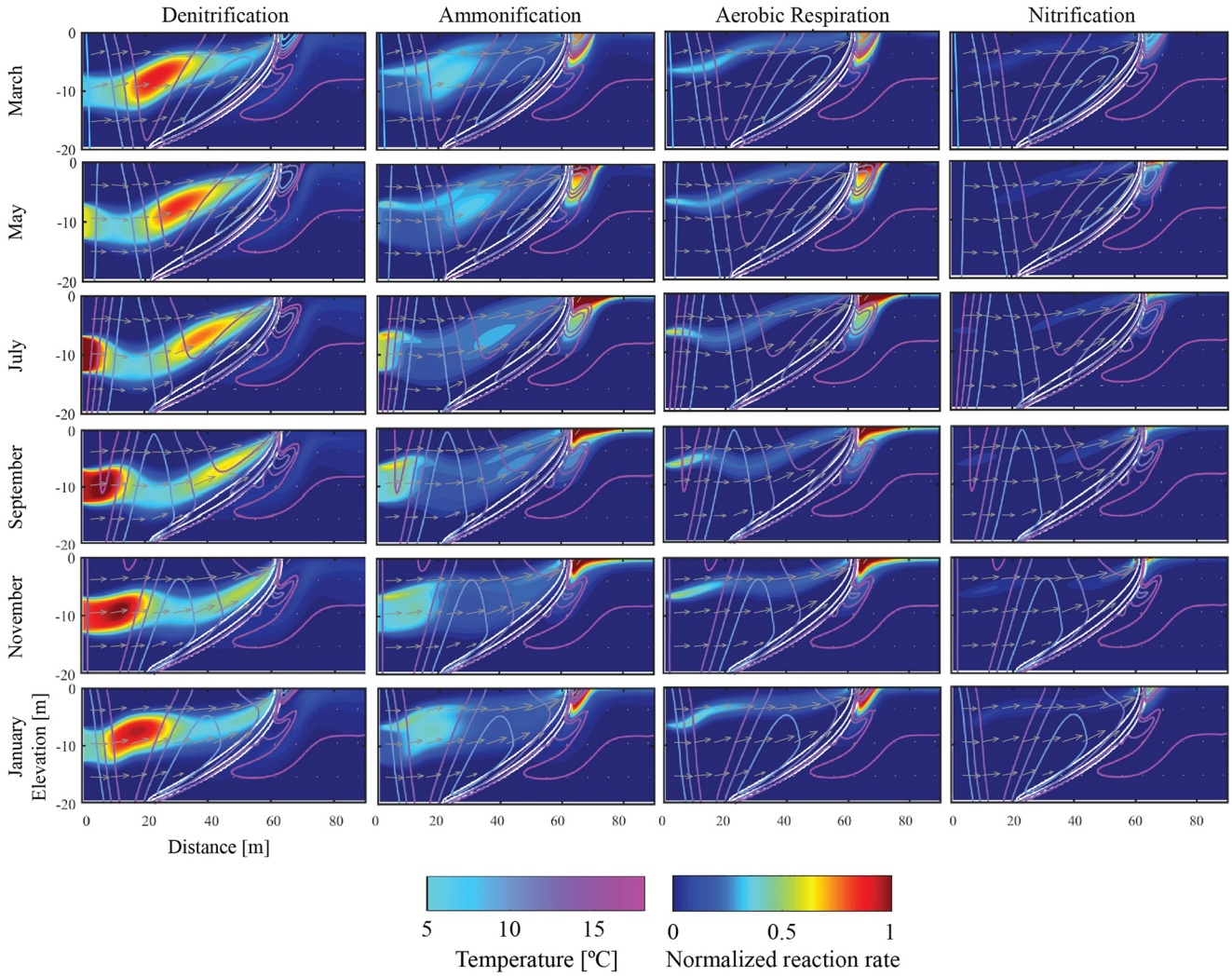

Figure 10. Bimonthly simulated reaction rates from the transient model. Light blue to purple contours correspond to temperature. Reaction hotspots are bracketed by high temperature contours as they travel through the aquifer. The white contours are the 5%, 50%, and 95% seawater salinity contours. Reaction rates are normalized by the maximum reaction rate. The gray vectors show the flow field.

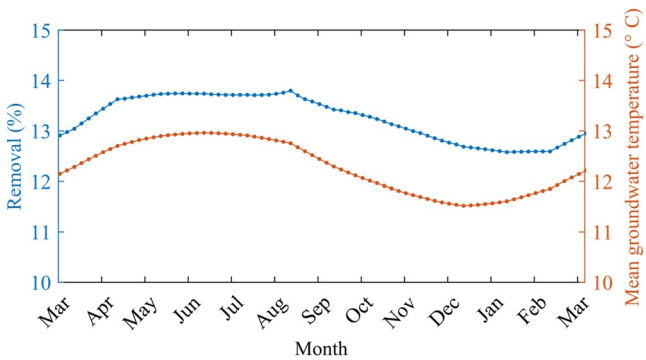

Figure 11. NO_3^- removal efficiency and mean fresh groundwater temperature over a period of one year.

4.3. Implications for Potential Reactivity Along the Global Coast

The model results (Figures 3–9) and the global variability in coastal groundwater and nearshore ocean temperature (see global temperature maps in Nguyen et al., 2020) suggest that for the model setup considered, the potential for coastal aquifers to process nutrients varies along the world coastline, with potential nitrate removal efficiencies of up to 88% at 35°C in the low latitudes and as low as 5% at 5°C in the far northern and southern hemispheres. Coastal aquifers at lower latitudes have a higher reactive potential owing to warmer groundwater temperatures. Coastal groundwater temperatures are highest along the Horn of Africa and northwest Australia 10–20° N/S of the equator, demonstrating the role of regional climate in determining groundwater temperature and hence the reactive potential of coastal groundwater systems in those regions.

Projections of nutrient enrichment in freshwater catchments show that North and South America and Europe are likely to suffer from algal growth associated with phosphorous enrichment. Africa, the Middle East, and India are

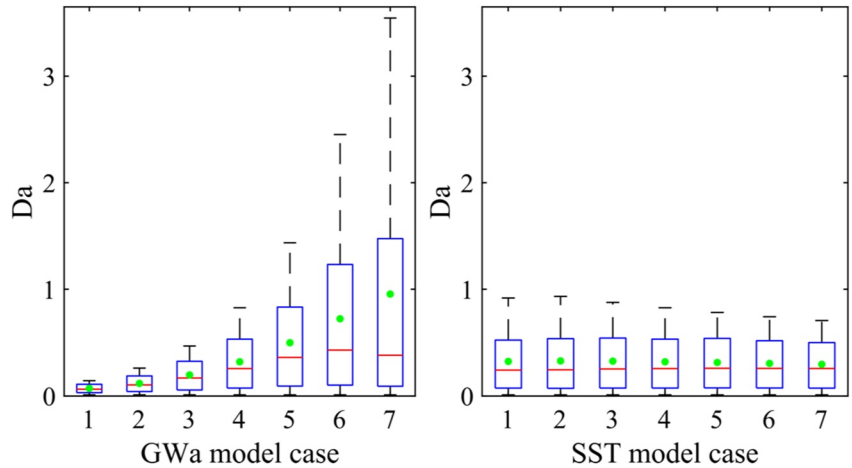

Figure 12. Summary statistics of *Da* within the denitrification zone for model sets GWa and SST. The red horizontal lines are the median, the green circles are the mean, the bottom and top edges of the boxes indicate the 25th and 75th percentiles, respectively, and the whiskers show the maximum and minimum values. Boxplots for model set GWb are nearly identical to GWa and are not shown.

projected to experience N enrichment and associated algal growth (McDowell et al., 2020). Nutrient enrichment of inland areas is likely to lead to increased nutrient loading to coastal aquifers, and subsequently, increased nutrient fluxes to coastal waters via submarine groundwater discharge. Our model results provide a first-order temperature-dependent estimate of the potential of coastal aquifers in these regions to attenuate N loads in fresh groundwater before discharging to the nearshore marine environment. Additionally, regions with large groundwater-ocean temperature contrasts are likely to host saltwater interfaces at different distances from the coast than for coastlines with the same fresh groundwater and seawater temperature. For instance, the cold California Current that flows south along the Pacific coast of North America forms larger temperature contrasts between fresh groundwater and seawater than for the same latitude on the Atlantic coast. In addition to affecting the inland extent of the interface toe (Pu et al., 2020), the results of this study suggest that such spatially variable temperature contrasts can influence the geometry of contaminant plumes in fresh groundwater flowing to the sea.

4.4. Implications for Climate Change

Climate change will affect groundwater temperatures due to an increase in the temperature of recharge (Burns et al., 2017) and from thermodynamic coupling between the atmosphere and ground (Hemmerle & Bayer, 2020). Coastal ocean temperatures will also increase due in part to shifts in ocean circulation patterns (Rahmstorf et al., 2015). Future warming of coastal fresh groundwater would likely lead to higher NO_3^- removal efficiencies and lower groundwater NO_3^- fluxes to coastal ecosystems, all else constant. Additionally, changes to groundwater and ocean temperatures lag climate change at different time scales (Burns et al., 2017; Hansen et al., 2005), which will generate conditions of nonuniform fresh groundwater and seawater temperatures. As discussed above, the models show that future inland shifts to the saltwater-freshwater interface that arises from nonuniform groundwater and coastal ocean temperature changes may displace seaward flowing chemical plumes upward, with implications for nutrient fluxes to coastal streams and lakes, as well as for contamination of pumping wells. Further, marine heat waves or periods of extreme high sea surface temperature relative to the long-term seasonal cycle (Hobday et al., 2016) are increasing in frequency due to anthropogenic warming (IPCC, 2019) and are becoming more intense and longer (Frölicher & Laufkötter, 2018; Smale et al., 2019; Laufkötter et al., 2020). These localized and intermittent seawater warming events would decrease the density ratio between seawater and fresh groundwater and may cause saltwater-freshwater interfaces to shift seaward. To characterize the influence of dynamic ocean warming events, future studies should consider interface response time scales relative to changes in sea surface temperature beyond seasonal cycles as considered in this study. Understanding long-term patterns in groundwater and coastal ocean temperature changes and corresponding lags to climate change will improve the understanding of future contaminant plume dynamics, biogeochemical processing rates in coastal porewater, and chemical fluxes to surface water.

Climate change models predict greater warming over land compared to oceans, with the greatest warming in the Arctic and midlatitudes in the northern hemisphere (Collins et. al, 2013) where warming may reach 4–7°C by 2100 under intermediate carbon emission scenarios (IPCC, 2018). Assuming the temperature of shallow groundwater increases by the same amount, our model sensitivity tests suggest that a 4–7°C increase of cooler fresh groundwater could translate to a 5-10% increase in bulk reactivity of coastal aquifers under the contamination scenario considered in this study. Thus, even if average global temperatures are held to 1.5–2°C, spatially nonuniform heating on land and Arctic amplification are likely to affect groundwater chemical loads to coastal systems through temperature controls on porewater reaction kinetics.

4.5. Model Assumptions and Considerations

We used a simplified model setup to isolate the effects of temperature on biogeochemical transformations in coastal aquifers. The models assumed homogeneous aquifer material; however, sediment heterogeneity is ubiquitous in coastal environments (Holland & Elmore, 2008). Heterogeneity in hydraulic conductivity creates preferential flow paths that affect the width, inland extent, and configuration of the saltwater interface (Michael et al., 2016). Groundwater pumping in heterogeneous coastal aquifers introduces additional complexity in saltwater-freshwater mixing patterns (Yu & Michael, 2019). Changes to freshwater flow paths along the saltwater interface due to geologic structures would affect contaminant plume migration, residence times, and chemical processing. Geologic heterogeneity can also enhance NO_3^- removal in intertidal saltwater-freshwater mixing zones (Heiss & Michael, 2020) and in the banks of tidal rivers (Wallace et al., 2020). These geologic controls on solute transport, mixing, and reactivity would lead to more complex biogeochemical responses than simulated in this study. Future studies should consider the influence of sediment composition and continuity on temperature-dependent nutrient cycling along the saltwater-freshwater interface. Further, chemical heterogeneity in the form of seawater-derived particulate organic carbon (Kim et al., 2020) and in situ buried wrack (Heiss, 2020) can serve as a carbon source to support coastal aquifer reactivity. However, these additional carbon sources are likely minimal inland from the shoreline.

The models did not include tidal fluctuations and therefore omit chemical processing in the intertidal saltwater circulation cell. Seawater infiltrating across the beachface due to tidal action introduces DOC into intertidal sediments (Beck et al., 2017; Ullman et al., 2003), which supports the consumption of NO_3^- in fresh groundwater flowing through the beach aquifer (Couturier et al., 2017). NO_3^- removal efficiency in intertidal aquifers under tidal influence can span from 20 to 100% (Anwar et al., 2014; Heiss et al., 2017), depending on tidal amplitude and beach properties. The present study shows that temperature can have a similar effect on the range of NO_3^- removal efficiencies along the saltwater interface, with NO_3^- removal efficiencies ranging from 5 to 88%. While the ranges are similar, total removal is lower along the lower interface compared to intertidal circulation cells, suggesting that N reactivity supported by tides may be more important than redox processes along the saltwater interface for the model setup considered in this study.

The transient model did not consider seasonal oscillations in the freshwater hydraulic gradient that cause alternating fresh and saline fluxes across the sea floor (Michael et al., 2005). An oscillating freshwater hydraulic gradient would affect the residence time of freshwater flowing from upland to the discharge zone, influencing the extent of time solutes that may undergo chemical processing. However, these impacts may be minimal for topography-limited systems that cover 70% of the world coastline (Michael et al., 2013). The effects of seasonal sea level anomalies on the position of the saltwater interface (Gonneea et al., 2013) were also not incorporated into the transient model to isolate temperature influences. Like seasonal variability in recharge, changes in sea level control the freshwater hydraulic gradient and would likely have similar effects on residence times and aquifer reactivity.

The boundary conditions and specified distribution of inflowing solutes used in our models are representative of a coastal aquifer in the Northeastern United States (Spiteri, Slomp, Tuncay, et al., 2008; Kreoger et al., 2007); however, the vertical extent and overlap of chemical plumes flowing to the coast are geographically variable (e.g., Santos et al., 2008). A variety of transport boundary conditions that represent other contaminant scenarios would allow for a more comprehensive characterization of the role of porewater temperature on nutrient transport behavior and chemical transformation in these systems.

5. Conclusions

In this study, we investigated the role of global and seasonal variability in groundwater and coastal ocean temperatures on spatial and temporal trends in N cycling in coastal aquifers. Numerical variable-density groundwater flow, heat transport, and reactive transport models were used to explore the complex interactions between solute transport, thermally controlled buoyancy, and temperature-dependent biogeochemical processing. The model results are the first to systematically show the effects of temperature on biogeochemical processing in coastal aquifers. We performed a sensitivity analysis of the reactive potential of coastal aquifers across the range of thermal conditions that exist between groundwater and the ocean along the global coast. The results show that temperature strongly controls aerobic respiration, denitrification, and nitrification rates in fresh and saline porewater.

In steady-state models, NO_3^- removal efficiency increased from 5% to 88% as fresh groundwater temperature increased from 5°C to 35°C due to the influence of temperature on the kinetic energy of reactants, while seawater temperature exerted negligible control over denitrification. However, seawater temperature affected the geometry and depth of contaminant plumes in the fresh groundwater by influencing the position of the saltwater interface through the density contrast between seawater and fresh groundwater.

We performed a transient one-year simulation that incorporated monthly groundwater and bay water temperature measurements from Waquoit Bay National Estuarine Research Reserve located on Cape Cod, Massachusetts, USA. The model showed that seasonal variability in fresh groundwater temperature can affect solute transport paths, the structure of contaminant plumes, and porewater NO_3^- removal efficiency. Warm groundwater masses that entered the freshwater aquifer in summer migrated seaward in seaward flowing groundwater and hosted denitrification and ammonification hotspots. Density contrasts between warm and cold fresh groundwater masses led to undulating transport paths due to thermally controlled buoyancy. Model comparisons showed that mean annual fresh groundwater and ocean temperatures can be incorporated as end-members in steady-state models of coastal aquifers when estimating annually averaged NO_3^- removal efficiency.

The results of this study can be used to inform the timing and location of field measurements and can aid in extrapolating incubated laboratory reaction rates over time and space. The findings have implications for understanding regional variability in groundwater nutrient loads to coastal ecosystems and for predicting saltwater-freshwater interface and porewater biogeochemical responses to a warming ocean and climate.

Data Availability Statement

The data necessary to reproduce the findings of this manuscript are available on CAUSHI HydroShare (Cogswell, 2021).

Acknowledgments
We thank two anonymous reviewers for suggestions and comments that greatly improved the manuscript. We also thank Christopher Russoniello for valuable discussions that strengthened this work, and Bryce Mase for assistance in the field. J.H was supported by the National Science Foundation grant EAR1933058.

References

Addy, K., Gold, A., Nowicki, B., McKenna, J., Stolt, M., & Groffman, P. (2005). Denitrification capacity in a subterranean estuary below a Rhode Island fringing salt marsh. *Estuaries*, *28*, 896–908. https://doi.org/10.1007/bf02696018

Ahrens, J., Beck, M., Marchant, H. K., Ahmerkamp, S., Schnetger, B., & Brumsack, H. J. (2020). Seasonality of Organic Matter Degradation Regulates Nutrient and Metal Net Fluxes in a High Energy Sandy Beach. *Journal of Geophysical Research: Biogeosciences*, *125*(2). https://doi.org/10.1029/2019JG005399

Anwar, N., Robinson, C., & Barry, D. A. (2014). Influence of tides and waves on the fate of nutrients in a nearshore aquifer: Numerical simulations. *Advances in Water Resources*, *73*, 203–213. https://doi.org/10.1016/j.advwatres.2014.08.015

Beck, M., Reckhardt, A., Amelsberg, J., Bartholomä, A., Brumsack, H. J., Cypionka, H., et al. (2017). The drivers of biogeochemistry in beach ecosystems: A cross-shore transect from the dunes to the low-water line. *Marine Chemistry*, *190*, 35–50. https://doi.org/10.1016/j.marchem.2017.01.001

Benz, S. A., Bayer, P., & Blum, P. (2017). Global patterns of shallow groundwater temperatures. *Environmental Research Letters*, *12*(3), 034005. https://doi.org/10.1088/1748-9326/aa5fb0

Bokuniewicz, H. J. (1992). Analytical descriptions of subaqueous groundwater seepage. *Estuaries*, *15*(4), 458–464. https://doi.org/10.2307/1352390

Burnett, B. (1999). Offshore springs and seeps are focus of working group. *Eos Trans. AGU*, *80*(2), 13–15. https://doi.org/10.1029/99EO00014

Burns, E. R., Zhu, Y., Zhan, H., Manga, M., Williams, C. F., Ingebritsen, S. E., & Dunham, J. B. (2017). Thermal effect of climate change on groundwater-fed ecosystems. *Water Resources Research*, *53*, 3341–3351. https://doi.org/10.1002/2016wr020007

Charbonnier, C., Anschutz, P., Deflandre, B., Bujan, S., & Lecroart, P. (2016). Measuring pore water oxygen of a high-energy beach using buried probes. *Estuarine, Coastal and Shelf Science*, *179*, 66–78. https://doi.org/10.1016/j.ecss.2015.12.004

Charbonnier, C., Anschutz, P., Poirier, D., Bujan, S., & Lecroart, P. (2013). Aerobic respiration in a high-energy sandy beach. *Marine Chemistry*, *155*, 10–21. https://doi.org/10.1016/j.marchem.2013.05.003

Charbonnier, C., Lavesque, N., Anschutz, P., Bachelet, G., & Lecroart, P. (2016). Role of macrofauna on benthic oxygen consumption in sandy sediments of a high-energy tidal beach. *Continental Shelf Research*, *120*, 96–105. https://doi.org/10.1016/j.csr.2016.03.017

Cogswell, C. (2021). *Model and Figure Data for "Climate and Seasonal Temperature Controls on Biogeochemical Transformations in Unconfined Coastal Aquifers*. HydroShare. http://www.hydroshare.org/resource/75bc2b215d9f4e99b0d9a4a0aeb9ce18

Collins, M., Knutti, R., Arblaster, J., Dufresne, J.-L., Fichefet, T., Friedlingstein, P., et al. (2013). Long-term Climate Change: Projections, Commitments and Irreversibility. In T. F. Stocker, D. Qin, G.-K. Plattner, M. Tignor, S. K. Allen, J. Boschung, et al. (Eds.), *Climate Change 2013: The Physical Science Basis. Contribution of Working Group I to the Fifth Assessment Report of the Intergovernmental Panel on Climate Change*. Cambridge University Press.

Couturier, M., Tommi-Morin, G., Sirois, M., Rao, A., Nozais, C., & Chaillou, G. (2017). Nitrogen transformations along a shallow subterranean estuary. *Biogeosciences*, *14*(13), 3321–3336. https://doi.org/10.5194/bg-14-3321-2017

Dawson, R., & Murphy, K. (1972). The temperature dependency of biological denitrification. *Water Resources Research*, *6*, 71–83. https://doi.org/10.1016/0043-1354(72)90174-1

Degenhardt, J., Dlugosch, L., Ahrens, J., Beck, M., Waska, H., & Engelen, B. (2020). Seasonal Dynamics of Microbial Diversity at a Sandy High Energy Beach Reveal a Resilient Core Community. *Frontiers in Marine Science*, *7*. https://doi.org/10.3389/fmars.2020.573570

Erler, D. V., Santos, I. R., Zhang, Y., Tait, D. R., Befus, K. M., Hidden, A., et al. (2014). Nitrogen transformations within a tropical subterranean estuary. *Marine Chemistry*, *164*, 38–47. https://doi.org/10.1016/j.marchem.2014.05.008

Frölicher, T. L., & Laufkötter, C. (2018). Emerging risks from marine heat waves. *Nat. Commun.*, *9*(2018), 650. https://doi.org/10.1038/s41467-018-03163-6

Gelhar, L. W., Welty, C., & Rehfeldt, K. R. (1992). A critical review of data on field-scale dispersion in aquifers. *Water Resources Research*, *28*(7), 1955–1974. https://doi.org/10.1029/92wr00607

Gonneea, M. E., & Charette, M. A. (2014). Hydrologic controls on nutrient cycling in an unconfined coastal aquifer. *Environmental Science and Technology*, *48*(24), 14178–14185. https://doi.org/10.1021/es503313t

Gonneea, M. E., Mulligan, A. E., & Charette, M. A. (2013). Climate-driven sea level anomalies modulate coastal groundwater dynamics and discharge. *Geophysical Research Letters*, *40*(11), 2701–2706. https://doi.org/10.1002/grl.50192

Grzelak, K., Tamborski, J., Kotwicki, L., & Bokuniewicz, H. (2018). Ecostructuring of marine nematode communities by submarine groundwater discharge. *Marine Environmental Research*, *136*(January), 106–119. https://doi.org/10.1016/j.marenvres.2018.01.013

Gu, C., Hornberger, G. M., Mills, A. L., Herman, J. S., & Flewelling, S. A. (2007). Nitrate reduction in streambed sediments: Effects of flow and biogeochemical kinetics. *Water Resources Research*, *43*(12), 1–10. https://doi.org/10.1029/2007WR006027

Guo, X., Xu, B., Burnett, W. C., Wei, Q., Nan, H., Zhao, S., et al. (2020). Does submarine groundwater discharge contribute to summer hypoxia in the Changjiang (Yangtze) River Estuary?. *Science of the Total Environment*, *719*, 137450. https://doi.org/10.1016/j.scitotenv.2020.137450

Hansen, J., Nazarenko, L., Ruedy, R., Sato, M., Willis, J., Del Genio, A., et al. (2005). Earth's Energy Imbalance: Confirmation and Implications. *Science*, *308*(5727), 1431–1435. https://doi.org/10.1126/science.1110252

Harbaugh, A. W., Banta, E. R., Hill, M. C., Mcdonald, M. G., & Groat, C. G. (2000). *MODFLOW-2000, The U.S. Geological Survey Modular Groundwater Model User Guide to Modularization Concepts and the Groundwater Flow Process U.S. Geological Survey, Open-File Report 00-92*. U.S. Department of the Interior. User Guide to Modularization Concepts and the Ground-Water Flow Process.

Hemmerle, H., & Bayer, P. (2020). Climate Change Yields Groundwater Warming in Bavaria, Germany. *Frontiers in Earth Science*, *8*, 1–8. https://doi.org/10.3389/feart.2020.575894

Heiss, J. W. (2020). Whale burial and organic matter impacts on biogeochemical cycling in beach aquifers and leachate fluxes to the nearshore zone. *Journal of Contaminant Hydrology*, *233*, 103656. https://doi.org/10.1016/j.jconhyd.2020.103656

Heiss, J. W., Michael, H. A., & Koneshloo, M. (2020). Denitrification hotspots in intertidal mixing zones linked to geologic heterogeneity. *Environmental Research Letters*, *15*(8), 084015. https://doi.org/10.1088/1748-9326/ab90a6

Heiss, J. W., Post, V. A. E., Laattoe, T., Russoniello, C. J., & Michael, H. A. (2017). Physical controls on biogeochemical processes in intertidal zones of beach aquifers, *Water Resources Research*, *53*, 9225–9244. https://doi.org/10.1002/2017WR021110

Hobday, A. J., Alexander, L. V., Perkins, S. E., Smale, D. A., Straub, S. C., Oliver, E. C. J., et al. (2016). A hierarchical approach to defining marine heatwaves. *Progress in Oceanography*, *141*, 227–238. https://doi.org/10.1016/j.pocean.2015.12.014

Holland, K. T., & Elmore, P. A. (2008). A review of heterogeneous sediments in coastal environments. *Earth-Science Reviews*, *89*(3–4), 116–134. https://doi.org/10.1016/j.earscirev.2008.03.003

Hughes, J. D., Sanford, W. E., & Sanford, W. E. (2004). *SUTRA-MS: A version of SUTRA modified to simulate heat and multiple-solute transport* (p. 141). U.S. Geological Survey Open-File Report 2004–1207. https://doi.org/10.3133/ofr20041207

IPCC. (2018). In T. F. Stocker, D. Qin, G.-K. Plattner, M. Tignor, S. K. Allen, J. Boschung, et al. (Eds.), *Climate Change 2013: The Physical Science Basis. Contribution of Working Group I to the Fifth Assessment Report of the Intergovernmental Panel on Climate Change* (p. 1535). Cambridge University Press.

IPCC. (2019). In H.-O. Pörtner, D. C. Roberts, V. Masson-Delmotte, P. Zhai, M. Tignor, E. Poloczanska, et al. (Eds.), *IPCC Special Report on the Ocean and Cryosphere in a Changing Climate*. In press.

Kim, K., & Heiss, J. (2021). Methods in Capturing the Spatiotemporal Dynamics of Flow and Biogeochemical Reactivity in Sandy Beach Aquifers: A Review. *Water*, *13*(6), 782. https://doi.org/10.3390/w13060782

Kim, K. H., Heiss, J. W., Geng, X., & Michael, H. A. (2020). Modeling Hydrologic Controls on Particulate Organic Carbon Contributions to Beach Aquifer Biogeochemical Reactivity. *Water Resources Research*, *56*(10), 1–17. https://doi.org/10.1029/2020WR027306

Kim, K. H., Heiss, J. W., Michael, H. A., Cai, W. J., Laattoe, T., Post, V. E. A., & Ullman, W. J. (2017). Spatial Patterns of Groundwater Biogeochemical Reactivity in an Intertidal Beach Aquifer. *Journal of Geophysical Research: Biogeosciences*, *122*(10), 2548–2562. https://doi.org/10.1002/2017JG003943

Knights, D., Sawyer, A. H., Barnes, R. T., Musial, C. T., & Bray, S. (2017). Tidal controls on riverbed denitrification along a tidal freshwater zone. *Water Resources Research*, *53*, 799–816. https://doi.org/10.1002/2016wr019405

Kroeger, K. D., & Charette, M. A. (2008). Nitrogen biogeochemistry of submarine groundwater discharge. *Limnology and Oceanography*, *53*(3), 1025–1039. https://doi.org/10.4319/lo.2008.53.3.1025

Kroeger, K. D., Swarzenski, P. W., Greenwood, W. J., & Reich, C. (2007). Submarine groundwater discharge to Tampa Bay : Nutrient fluxes and biogeochemistry of the coastal aquifer. *Marine Chemistry*, *104*, 85–97. https://doi.org/10.1016/j.marchem.2006.10.012

Langevin, C. D., Thorne, D. T., Dausman, A. M., Sukop, M. C., & Guo, W. (2007). *SEAWAT Version 4: A Computer Program for Simulation of Multi-Species Solute and Heat Transport*. U.S. Geological Survey. (Technical Report, U.S. Geological Survey Techniques and Methods Book 6, Chapter A22, 39 pp.).

Laufkötter, C., Zscheischler, J., & Frölicher, T. L. (2020). High-impact marine heatwaves attributable to human-induced global warming. *Science*, *369*(6511), 1621–1625. LP – 1625. https://doi.org/10.1126/science.aba0690

Lecher, A. L., Mackey, K., Kudela, R., Ryan, J., Fisher, A., Murray, J., & Paytan, A. (2015). Nutrient loading through submarine groundwater discharge and phytoplankton growth in Monterey bay, CA. *Environmental Science and Technology*, *49*(11), 6665–6673. https://doi.org/10.1021/acs.est.5b00909

Locarnini, R. A., Mishonov, A. V., Antonov, J. I., Boyer, T. P., Garcia, H. E., Baranova, O. K., et al. (2013). World Ocean Atlas 2013, Volume 1: Temperature. In S. Levitus, A. Mishonov, & Technical (Eds.), *NOAA Atlas NESDIS* (Vol. 73, p. 40).

Luijendijk, E., Gleeson, T., & Moosdorf, N. (2020). Fresh groundwater discharge insignificant for the world's oceans but important for coastal ecosystems. *Nature Communications*, *11*(1). https://doi.org/10.1038/s41467-020-15064-8

McDowell, R. W., Noble, A., Pletnyakov, P., Haggard, B. E., & Mosley, L. M. (2020). Global mapping of freshwater nutrient enrichment and periphyton growth potential. *Scientific Reports*, *10*(1), 1–13. https://doi.org/10.1038/s41598-020-60279-w

Michael, H. A., Mulligan, A. E., & Harvey, C. F. (2005). Seasonal oscillations in water exchange between aquifers and the coastal ocean. *Nature*, *436*(7054), 1145–1148. https://doi.org/10.1038/nature03935

Michael, H. A., Russoniello, C. J., & Byron, L. (2013). Global assessment of vulnerability to sea-level rise in topography-limited and recharge-limited coastal groundwater systems. *Water Resources Research*, *49*(4), 2228–2240. https://doi.org/10.1002/wrcr.20213

Michael, H. A., Scott, K. C., Koneshloo, M., Yu, X., Khan, M. R., & Li, K. (2016). Geologic influence on groundwater salinity drives large seawater circulation through the continental shelf. *Geophysical Research Letters*, *43*(20), 10782–10791. https://doi.org/10.1002/2016GL070863

Molz, F. J., Widdowson, M. A., & Benefield, L. D. (1986). Simulation of microbial growth dynamics coupled to nutrient and oxygen trans- port in porous media. *Water Resources Research*, *22*(8), 1207–1216. https://doi.org/10.1029/WR022i008p01207

Moore, W. S. (1999). The subterranean estuary: A reaction zone of ground water and sea water. *Marine Chemistry*, *65*(1–2), 111–125. https://doi.org/10.1016/S0304-4203(99)00014-6

Mulligan, A. E., & Charette, M. A. (2006). Intercomparison of submarine groundwater discharge estimates from a sandy unconfined aquifer. *Journal of Hydrology*, *327*(3–4), 411–425. https://doi.org/10.1016/j.jhydrol.2005.11.056

Nguyen, T. T. M., Yu, X., Pu, L., Xin, P., Zhang, C., Barry, D. A., & Li, L. (2020). Effects of Temperature on Tidally Influenced Coastal Unconfined Aquifers. *Water Resources Research*, *56*(4), 1–17. https://doi.org/10.1029/2019WR026660

Paerl, H. W. (1997). Coastal eutrophication and harmful algal blooms: Importance of atmospheric deposition and groundwater as new nitrogen and other nutrient sources. *Limnology and Oceanography*, *42*(5_part_2), 1154–1165. https://doi.org/10.4319/lo.1997.42.5_part_2.1154

Pisternick, T., Lilkendey, J., Audit-Manna, A., Dumur Neelayya, D., Neehaul, Y., & Moosdorf, N. (2020). Submarine groundwater springs are characterized by distinct fish communities. *Marine Ecology*, *41*(May), 1–15. https://doi.org/10.1111/maec.12610

Prommer, H., & Post, V. (2002). A reactive multicomponent transport model for saturated porous media. In *Contaminated Land Assessment and Remediation Research Centre*. The University of Edinburgh, Edinburgh, UK.

Pu, L., Xin, P., Nguyen, T. T. M., Yu, X., Li, L., & Barry, D. A. (2020). Thermal Effects on Flow and Salinity Distributions in Coastal Confined Aquifers. *Water Resources Research*, *56*(10), 1–17. https://doi.org/10.1029/2020WR027582

Rahmstorf, S., Box, J. E., Feulner, G., Mann, M. E., Robinson, A., Rutherford, S., & Schaffernicht, E. J. (2015). Exceptional twentieth-century slowdown in Atlantic Ocean overturning circulation. *Nature Climate Change*, *5*(5), 475–480. https://doi.org/10.1038/nclimate2554

Rutkowski, C.M., Burnett, W.C., Iverson, R.L., & Chanton, J. P. (1999). The effect of groundwater seepage on nutrient delivery and seagrass distribution in the northeastern Gulf of Mexico. *Estuaries*, *22*, 1033–1040. https://doi.org/10.2307/1353081

Santos, I. R., Burnett, W. C., Chanton, J., Mwashote, B. M., Suryaputra, I. G. N. A., & Dittmar, T. (2008). Nutrient biogeochemistry in a Gulf of Mexico subterranean estuary and groundwater-derived fluxes to the coastal ocean. *Limnology and Oceanography*, *53*(2), 705–718. https://doi.org/10.4319/lo.2008.53.2.0705

Sheibley, R. W., Jackman, A. P., Duff, J. H., & Triska, F. J. (2003). Numerical modeling of coupled nitrification-denitrification in sediment perfusion cores from the hyporheic zone of the Shingobee River, MN. *Advances in Water Resources*, *26*(9), 977–987. https://doi.org/10.1016/S0309-1708(03)00088-5

Slomp, C. P., & Van Cappellen, P. (2004). Nutrient inputs to the coastal ocean through submarine groundwater discharge: Controls and potential impact. *Journal of Hydrology*, *295*(1–4), 64–86. https://doi.org/10.1016/j.jhydrol.2004.02.018

Smale, D.A., Wernberg, T., Oliver, E.C.J., Thomsen, M., Harvey, B. P., Straub, S. C., et al. (2019). Marine heatwaves threaten global biodiversity and the provision of ecosystem services. *Nat. Clim. Chang.*, *9*, 306–312. https://doi.org/10.1038/s41558-019-0412-1

Spiteri, C., Slomp, C. P., Charette, M. A., Tuncay, K., & Meile, C. (2008). Flow and nutrient dynamics in a subterranean estuary (Waquoit Bay, MA, USA): Field data and reactive transport modeling. *Geochimica et Cosmochimica Acta*, *72*(14), 3398–3412. https://doi.org/10.1016/j.gca.2008.04.027

Spiteri, C., Slomp, C. P., Tuncay, K., & Meile, C. (2008). Modeling biogeochemical processes in subterranean estuaries: Effect of flow dynamics and redox conditions on submarine groundwater discharge of nutrients. *Water Resources Research*, *44*(2). https://doi.org/10.1029/2007WR006071

Talbot, J. M., Kroeger, K. D., Rago, A., Allen, M. C., & Charette, M. A. (2003). Nitrogen flux and speciation through the subterranean estuary of Waquoit Bay, Massachusetts. *The Biological Bulletin*, *205*(2), 244–245. https://doi.org/10.2307/1543276

Tamborski, J. J., Cochran, J. K., & Bokuniewicz, H. J. (2017). Submarine groundwater discharge driven nitrogen fluxes to Long Island Sound, NY: Terrestrial vs. marine sources. *Geochimica et Cosmochimica Acta*, *218*, 40–57. https://doi.org/10.1016/j.gca.2017.09.003

Tanaguchi, M., Burnett, W. C., Cable, J. E., & Turner, J. V. (2002). Investigation of submarine groundwater discharge. *Hydrol. Process.*, *16*, 2115–2129. https://doi.org/10.1002/hyp.1145

Thorne, D., Langevin, C. D., & Sukop, M. C. (2006). Addition of simultaneous heat and solute transport and variable fluid viscosity to SEAWAT. *Computers and Geosciences*, *32*(10), 1758–1768. https://doi.org/10.1016/j.cageo.2006.04.005

Ullman, W. J., Chang, B., Miller, D. C., & Madsen, J. A. (2003). Groundwater mixing, nutrient diagenesis, and discharges across a sandy beachface, Cape Henlopen, Delaware (USA). Estuarine. *Coastal and Shelf Science*, *57*(3), 539–552. https://doi.org/10.1016/s0272-7714(02)00398-0

Vandenbohede, A., & Lebbe, L. (2011). Heat transport in a coastal groundwater flow system near De Panne, Belgium. *Hydrogeology Journal*, *19*(2011), 1225–1238. https://doi.org/10.1007/s10040-011-0756-8

Voss, C. I., & Provost, A. M. (2010). SUTRA: A model for saturated-unsaturated, variable-density ground-water flow with solute or energy transport. *Water-Resources Investigation Rep, 02-4231*, 300.

Wallace, C. D., Sawyer, A. H., Soltanian, M. R., & Barnes, R. T. (2020). Nitrate Removal Within Heterogeneous Riparian Aquifers Under Tidal Influence. *Geophysical Research Letters*, *47*(10). https://doi.org/10.1029/2019GL085699

Waska, H., Greskowiak, J., Ahrens, J., Beck, M., Ahmerkamp, S., Böning, P., et al. (2019). Spatial and Temporal Patterns of Pore Water Chemistry in the Inter-Tidal Zone of a High Energy Beach. *Frontiers in Marine Science*, *6*(April), 1–16. https://doi.org/10.3389/fmars.2019.00154

Widdowson, M. A., Molz, F. J., & Benefield, L. D. (1988). A numerical transport model for oxygen- and nitrate-based respiration linked to substrate and nutrient availability in porous media. *Water Resources Research*, *24*(9), 1553–1565. https://doi.org/10.1029/WR024i009p01553

Yu, X., & Michael, H. A. (2019). Mechanisms, configuration typology, and vulnerability of pumping-induced seawater intrusion in heterogeneous aquifers. *Advances in Water Resources*, *128*(April), 117–128. https://doi.org/10.1016/j.advwatres.2019.04.013

Zarnetske, J. P., Haggerty, R., Wondzell, S. M., Bokil, V. A., & González-Pinzón, R. (2012). Coupled transport and reaction kinetics control the nitrate source-sink function of hyporheic zones. *Water Resources Research*, *48*(11), 1–15. https://doi.org/10.1029/2012WR011894

Zheng, C., & Wang, P. P. (1999). *MT3DMS: A modular three- dimensional multispecies transport model for simulation of advection, dispersion, and chemical reactions of contaminants in ground water systems; Documentation and User's Guide*. U.S. Army Corps of Engineers Contract Report SERD-99-1.

Zheng, L., Cardenas, M. B., & Wang, L. (2016). Temperature effects on nitrogen cycling and nitrate removal-production efficiency in bed form-induced hyporheic zones. *Journal of Geophysical Research G: Biogeosciences*, *121*(4), 1086–1103. https://doi.org/10.1002/2015JG003162